



Research Article

GaLactic and Extragalactic All-sky Murchison Widefield Array eXtended (GLEAM-X) survey II: Second Data Release

Kathryn Ross¹, Natasha Hurley-Walker¹, Timothy James Galvin^{1,2}, Brandon Venville¹, Stefan William Duchesne², John Morgan^{1,2}, Tao An³, Gulay Gürkan^{4,2}, Paul J. Hancock^{1,5}, George Heald², Melanie Johnston-Hollitt⁵ and Sarah V. White^{1,6}

¹International Centre for Radio Astronomy Research, Curtin University, Bentley, WA, Australia, ²CSIRO Space & Astronomy, Bentley, WA, Australia, ³Shanghai Astronomical Observatory, Chinese Academy of Sciences, Shanghai, China, ⁴Centre for Astrophysics Research, University of Hertfordshire, College Lane, Hatfield AL10 9AB, UK, ⁵Curtin Institute for Data Science, Curtin University, Perth, WA, Australia and ⁶South African Astronomical Observatory, Cape Town, South Africa

Abstract

We present the second data release for the GaLactic and Extragalactic All-sky Murchison Widefield Array eXtended (GLEAM-X) survey. This data release is an area of 12 892-deg² around the South Galactic Pole region covering 20 h40 m ≤ RA ≤ 6 h40 m, -90° ≤ Dec ≤ +30°. Observations were taken in 2020 using the Phase-II configuration of the Murchison Widefield Array (MWA) and covering a frequency range of 72–231 MHz with twenty frequency bands. We produce a wideband source finding mosaic over 170–231 MHz with a median root-mean-squared noise of 1.5^{+1.5}_{-0.5} mJy beam⁻¹. We present a catalogue of 624 866 components, including 562 302 components which are spectrally fit. This catalogue is 98% complete at 50 mJy, and a reliability of 98.7% at a 5 σ level, consistent with expectations for this survey. The catalogue is made available via Vizier, and the PASA datastore and accompanying mosaics for this data release are made available via AAO Data Central and SkyView.

Keywords: techniques: interferometric; galaxies: general; radio continuum: surveys

(Received 19 February 2024; revised 23 May 2024; accepted 7 June 2024)

1 Introduction

Wide-area radio sky surveys enable a range of science across the Universe, from the most nearby scales, for example, measuring the solar wind (Morgan et al. 2023), to our own Galaxy, for example, finding unexpected types of transient radio sources (Hurley-Walker et al. 2022b), to the extragalactic sky (White et al. 2020a,b), such as measurements and variability of radio galaxies (Ross et al. 2022) and galaxy clusters (Duchesne et al. 2020), the detection of cosmic magnetism (Vernstrom et al. 2021), precision magnetism studies (Riseley et al. 2018, 2020), and ultimately cosmology (Hale et al. 2024).

Building towards the Square Kilometre Array (SKA), a recent resurgence in low-frequency radio astronomy has seen a plethora of new wide-area radio sky surveys. Hurley-Walker et al. (2022a) (hereafter referred to as HW22) introduced the GaLactic and Extragalactic All-Sky MWA – eXtended (GLEAM-X) survey, using the Murchison Widefield Array (MWA; Tingay et al. 2013) in its ‘extended’ Phase-II configuration (Wayth et al. 2018; Beardsley et al. 2019) to survey the sky south of Declination +30° over 72–231 MHz, with a source finding image formed at ~56'' resolution. The authors also introduced the many other wide-area

surveys that formed the foundation for, were contemporaneous with, or preceded GLEAM-X. Adding to the recent plethora of data releases, this paper presents the second data release to the GLEAM-X survey, henceforth called GLEAM-X DRII, which will add to the scientific resources available to the astronomical community.

Since GLEAM-X was described, a multitude of new radio surveys of the sky have become available or have had new data releases. The LOw-Frequency Array (LOFAR; van Haarlem et al. 2013) has produced a second data release from the LOFAR Two-metre Sky Survey at 120–180 MHz (LoTSS; Shimwell et al. 2017, 2022), a first data release from the LOFAR Low-Band Array Sky Survey at 41–66 MHz (LoLSS; de Gasperin et al. 2021, 2023), and deep imaging towards the LOFAR Deep Fields (Best et al. 2023). Dish interferometers with phased-array feeds have enabled wide-area higher-frequency surveys, such as the Apertif imaging survey (Adams et al. 2022), and the Rapid Australian SKA Pathfinder Continuum Surveys (RACS), in both unpolarised and circular polarisation (McConnell et al. 2020; Duchesne et al. 2023), as well as early results from measuring linear polarisation (Thomson et al. 2023). MeerKAT has also produced L-band surveys over smaller areas at greater sensitivities, such as the MeerKAT Absorption Line Survey (MALS) data release I (MALS; Deka et al. 2023) and MIGHTEE (Heywood et al. 2022). The first data release from the MWA interplanetary scintillation (IPS) survey has also been released (Morgan, Chhetri, & Ekers 2022) which provides information on the sub-arcsecond structure of over 40,000 GLEAM sources.

Corresponding author: Kathryn Ross; Email: kathryn.ross@icrar.org

Cite this article: Ross K, Hurley-Walker N, Galvin T J, Venville B, Duchesne S W, Morgan J, An T, Gürkan G, Hancock P J, Heald G, Johnston-Hollitt M and White S V. (2024) GaLactic and Extragalactic All-sky Murchison Widefield Array eXtended (GLEAM-X) survey II: Second Data Release. *Publications of the Astronomical Society of Australia* 41, e054, 1–23. <https://doi.org/10.1017/pasa.2024.57>

While GLEAM-X is one of the several ongoing low-frequency surveys, it continues to play a unique role combining wide fractional bandwidth, low frequencies, and large sky coverage, particularly in the Southern sky. Covering Declinations up to $+30^\circ$, GLEAM-X is complimentary to Northern sky surveys, like LoTSS, and bridges the gap as a Southern sky survey until SKA-LOW. Likewise, the synergies between other higher-frequency Southern sky surveys like RACS will prove a powerful source for discovery and characterisation of spectral properties for large populations of radio sources. The increased sensitivity and resolution of GLEAM-X compared to the predecessor, GLEAM, establish GLEAM-X as an avenue for novel scientific outcomes that were not available with GLEAM alone.

This paper is presented with the following layout. In Section 2, we describe the observational strategy and specific observations processed for this data release. In Section 3, we outline the changes and improvements made to the GLEAM-X processing pipeline since the initial data release and survey description (Hurley-Walker et al. 2022a). The properties of the final images are outlined in Section 4. In Section 5, we describe the compact source catalogue produced for this work and quality of this catalogue. All the results are summarised in Section 6.

All positions given in this paper are in J2000 equatorial coordinates.

2 Observations

GLEAM-X utilised the drift scan observing technique, outlined by Wayth et al. (2015), but adapted to iterate over three hour angles (HA), $HA = 0 \text{ h}, \pm 1 \text{ h}$, proven to increase sensitivity (Franzen et al. 2021). GLEAM-X DRI comprised four drift scans at Declinations centred on -26° and covering $4 \text{ h} \leq RA \leq 13 \text{ h}$ with different HAs (Hurley-Walker et al. 2022a). Observations for GLEAM-X DRI adopt the same observing strategy and cover the South Galactic Pole (SGP) region, spanning $\sim 20 \text{ h} \leq RA \leq 6 \text{ h}$ and $Dec \leq +30^\circ$. GLEAM-X DRII consists of 28 drift scans, with seven Declination pointings ($+20^\circ$, $+1^\circ$, -12° , -26° , -40° , -55° , and -71°) and HAs $= 0 \text{ h}, \pm 1 \text{ h}$. Each Declination pointing had four dedicated observing nights separated by one week and were taken from 2020-09-28 to 2020-10-25. A summary of the nights that were included in this data release is presented in Table A1.

As outlined by HW22, observations were taken with an instantaneous bandwidth of 30.72-MHz and cycled through five frequency ranges, 72–103, 103–134, 139–170, 170–200, and 200–231 MHz, every two minutes. This data release is the combination of over 1 000 h of observations taken with the MWA and covers a sky area of $\approx 12\,892 \text{ sq.deg}$. The region of sky covered in this data release and in GLEAM-X DRI is presented in Fig. 1

3 Continuum pipeline

The data reduction process used for both this data release and GLEAM-X DRI is described in full by HW22. However, with the increased sky coverage of this data release, several improvements to the data processing were introduced to improve image quality for low elevation pointings and minimise contamination from bright radio sources. The updated GLEAM-X pipeline is publicly available on the GLEAM-X organisation GitHub^a and as a containerised pipeline that can be run on any platform with

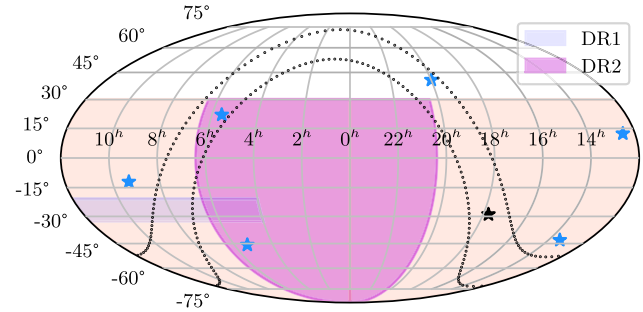


Figure 1. Sky coverage of the GLEAM-X survey. The blue region represents the area covered in the first data release (HW22), the region covered as part of this release is covered by the pink region and the total coverage of the GLEAM-X survey is shown by the cream region. The black star represents the Galactic centre and the black dotted lines represent the Galactic plane from $-10^\circ \leq b \leq 10^\circ$. The blue stars represent the bright A-team sources: Centaurus A, Crab, Cygnus A, Hydra A, Pictor A, and Virgo A.

Singularity installed (Kurtzer, Sochat, & Bauer 2017). Here we outline the changes to the reduction steps introduced in this data release. As the changes introduced in this data release are typically due to the increased Declination coverage (compared to GLEAM-X DRI where only zenith pointings were processed), the changes have been integrated into the GLEAM-X pipeline and will be implemented in future GLEAM-X data releases.

3.1 Calibration and improved sky model

We perform the same calibration approach as GLEAM-X DRI, by calibrating separately on individual 2-min snapshot observations in a direction-independent manner. A sky model is used that is primarily derived from GLEAM with additional models for complex sources. In this data release, we updated the model for Pictor-A with an improvement on the amplitude calibration, particularly for short baselines. The model for Pictor-A was derived from a combination of the Very Large Array (VLA) Sky Survey (VLASS; Lacy et al. 2020) and observations taken with MWA Phase-II as part of the GLEAM-X observing.

Calibration solutions from GLEAM-X observations that were near in time and pointing were applied to the observations of Pictor-A and then imaged using WSCLEAN (Offringa et al. 2014). A multi-component model of Pictor-A was derived with spectral indices calculated using all channels of the MWA and VLASS for each component. The final model comprised four components: two extended lobes with steep spectral indices and two hot spots with flat spectral indices.

3.2 Sidelobe subtraction

For observations taken at a low elevation, the sidelobe of the MWA primary beam has significant sensitivity that can cause imaging artefacts including alias sources from the sidelobe reflected into the main lobe. In this release, we introduce a sidelobe subtraction for observations where the sidelobe was more sensitive than 0.1% of the primary beam.^b

To reduce the sidelobe power, the visibilities are phase rotated to the sidelobe and then a shallow image is formed to create

^bThe mainlobe and sidelobe locations and sensitivities were calculated using `get_mwa_pb_lobes.py` as part of the SKYMODEL package available on GitHub: <https://github.com/Sunmish/skymodel>.

^a<https://github.com/GLEAM-X/GLEAM-X-pipeline>.

a model of the sidelobe. The shallow image is generated using WSCLEAN, using the following settings:

- imaging the XX, YY, XY, and YX instrumental polarisation with the cleaning performed on peaks calculated from the sum of the squares but subtracted from individual images using the `-join-polarizations` option;
- four 7.68 MHz channels are jointly cleaned for each polarisation product;
- a Briggs robust parameter of 0.5 (Briggs 1995);
- only one major clean cycle, where the images are inverse Fourier transformed back to visibilities and subtracted from the data;
- up to 4×10^4 minor cleaning cycles where subtractions are performed in the image plane rather than the visibilities;
- cleaning was stopped when negative components were reached

The ‘MODEL_DATA’ column of the observation measurement set was updated during this imaging, and subtracted from the visibilities after completion. The visibilities were then phase-rotated back to the mainlobe. This procedure is similar to the ‘demixing’ often used by LOFAR (van der Tol, Jeffs, & van der Veen 2007; Morabito et al. 2022), which also subtracts a bright off-axis nearby source from the data. However, demixing involves calibrating using a model for the source, which is then used to subtract the source from the data. In the sidelobe subtraction procedure introduced here, no calibration is derived or applied, a model of the sensitive sidelobe is produced via imaging and subtracted directly. This procedure dramatically reduced the overall power of the sidelobe sources in the visibilities, particularly for aliased sources (described further in Section 5.5), and ultimately resulted in a slight decrease to the final image root-mean-squared (RMS) noise level. Self-calibration was also applied to any observations that were identified as having significant sidelobes, this is described further in Section 3.3.

3.3 Self-calibration

For observations that were identified as having a significant sidelobe, a round of amplitude and phase self-calibration was applied. There was no noticeable improvement on image quality for observations that had no significant sidelobe contributions, thus self-calibration was not performed on these observations. Visibilities were phase-rotated back to the mainlobe pointing and another shallow imaging procedure was performed using WSCLEAN with the same imaging parameters as the shallow imaging for sidelobe subtraction outlined in Section 3.2. The ‘MODEL_DATA’ column of the observation measurement set was updated as part of the WSCLEAN imaging procedure. The ‘MODEL_DATA’ column was then used to calibrate using MITHCAL (Offringa et al. 2016). These calibration solutions were only applied if less than 20% of the solutions were flagged.

3.4 Ionospheric assessment

A final check of image quality was performed to identify any potential ionospheric effects resulting in significant blurring of sources in the image before combining snapshot images into the final mosaic. The blurring of sources from the ionosphere has a

larger impact on the lowest frequencies (i.e. 72–103 MHz), but the quality check was performed on all frequencies for consistency.

For each snapshot image, a quality control catalogue of sparse (no nearby sources within $1'$), unresolved in NRAO VLA Sky Survey (NVSS; Condon et al. 1998) and/or Sydney University Molonglo Sky Survey (SUMSS; Mauch et al. 2003), and high signal-to-noise (SNR ≥ 50) sources was produced and used for all further calculations. A source finding procedure is performed on each snapshot image using AEGEAN^c (Hancock et al. 2012; Hancock, Trott, & Hurley-Walker 2018), and a cross-match with the quality control catalogue was performed with $1'$ separation. Observations were flagged if there was fewer than 100 sources in the cross-match catalogue, or if the RMS noise level of the image were significantly higher (3σ) than the average RMS noise level for GLEAM-X images at the corresponding frequency band. The average and standard deviation of the ratio of integrated flux density to peak flux density ($S_{\text{int}}/S_{\text{peak}}$) of sources in the image were calculated for every observation for each night. Observations were flagged as having significant blurring if $S_{\text{int}}/S_{\text{peak}}$ had a mean ≥ 1.1 or a standard deviation ≥ 0.125 .

The mean and standard deviation of $S_{\text{int}}/S_{\text{peak}}$ were inspected for each observation over each observing night to identify any periods of high ionospheric activity or areas with poor image quality. The lowest frequency band (72–103 MHz) typically saw the largest number of observations flagged, which is expected since this frequency shows the greatest ionospheric blurring. However, the larger field of view also results in greater overlap between snapshot observations and thus minimal reduction in sensitivity in the final mosaic. This triage typically saw 10–15% of observations being flagged in the lowest frequency band in a night of observations and $<5\%$ for the higher-frequency bands, although up to 50% of observations were flagged in some nights with particularly large levels of ionospheric activity. Fig. 2 presents the mean $S_{\text{int}}/S_{\text{peak}}$ over a night of good ionospheric conditions and poor ionospheric conditions.

3.5 Combined multi-night mosaicking

The mosaicking procedure for individual nights followed the same routine that was outlined in GLEAM-X DRI. Individual snapshots were weighted according to the square of the primary beam model and the inverse square of the RMS of image. Snapshots were then co-added using SWARP (Bertin et al. 2002) and the point spread function (PSF) of the combined mosaic image was measured using the same approach as that outlined in GLEAM-X DRI. This resulted in a total of 26 mosaic images (20×7.68 -MHz frequency channel mosaic images, 5×30.72 -MHz mosaic images and a wideband 60-MHz image over 170–231 MHz) for each night of observations. However, for the Dec -71° drift scan, multiple nights had at least one frequency band that was of poor quality. Consequently, for the Dec -71° drift scan observations, instead of four nights each with 26 mosaics, observations from each night were combined in one step into 26 combined four-night mosaics.

The combined final mosaics for this data release were created by combining all 25 declination strips for each of the 20 7.68 MHz subband images and five 30.72 MHz images using SWARP. To optimise the SNR and ensure a smooth co-addition of the declination strips, weight maps were derived from the inverse square of the RMS maps as measured by BANE, a companion

^c<https://github.com/PaulHancock/Aegean>.

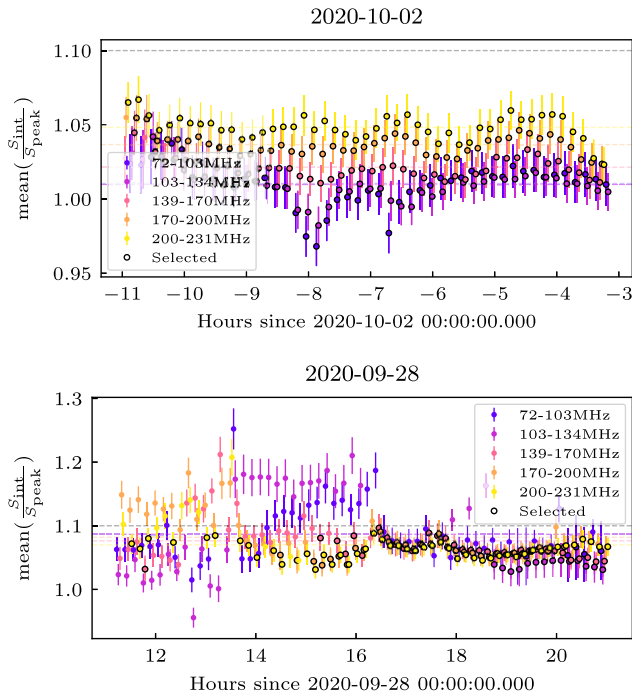


Figure 2. The mean ratio of integrated flux density to peak flux density, $S_{\text{int}}/S_{\text{peak}}$, for each 2 min snapshot observation over two nights of observing in this work. The top figure corresponds to 2020-10-02, a night identified as having good ionospheric conditions; and lower figure corresponds to 2020-09-28, a night identified as having poor ionospheric conditions. Horizontal lines of the same colours represent the median value for $S_{\text{int}}/S_{\text{peak}}$ for the corresponding channel over the night. The horizontal grey dashed line is the limit of 1.1 for $S_{\text{int}}/S_{\text{peak}}$ above which observations are discarded as having large ionospheric blurring. Points with a black outline are those that were selected as passing the ionospheric analysis and were included in mosaics for this release.

tool of AEGEAN. Weight maps were also calculated based on a declination-dependent sigmoid function to downweight the edges of the mosaics and minimise artefacts between the different declination strips. The 170–200 MHz and 200–231 MHz images were re-gridded and convolved to a common resolution and combined using SWARP to create the deep 60 MHz wideband image used for source finding.

3.6 Noise analysis

Here we analyse the noise properties of the source finding 170–231 MHz image and assess the impacts of confusion. We follow the noise analyses of GLEAM-X DRI and Hurley-Walker *et al.* (2017) on a 25 deg² region centred on RA 2^h30^m Dec−40°00′ as a representative region with typical source distribution and noise properties. The background and RMS maps are measured using BANE and the background is subtracted from the image. An initial source finding routine using AEGEAN, is used to detect sources down to 0.2× the local RMS noise level. These sources are either masked or subtracted from the background-subtracted image using AERES from the AEGEAN package. In Fig. 3, we present the histogram of the pixel distribution for the background subtracted, masked, and source subtracted images.

As discussed in HW22, a survey approaching the confusion limit will skew towards a positive distribution. However, for the wideband source finding image, the distribution is almost entirely symmetrical. The higher resolution of GLEAM-X compared to

GLEAM means confusion contributes a smaller fraction to the noise (Franzen *et al.* 2019). However, at the lowest frequency band of GLEAM-X, 72–103 MHz, the lower resolution means confusion is contributing a significant fraction to the noise levels. Consequently, BANE is unable to accurately measure the noise levels across the entire mosaic in the lowest frequency band. While the lowest frequency images of GLEAM-X are close to the confusion limit, the higher resolution of the higher-frequency images provides sufficient information to reduce the contribution of confusion to the final noise maps. The contribution of confusion to the noise levels at the wideband source finding image is minimal, so we use the source positions from the wideband catalogue for the prioritised fitting routine of AEGEAN.

For the 72–103 MHz image and the four 7.68 MHz subband images, an initial round of source finding using AEGEAN with the wideband catalogue as a prior for source positions was conducted. This catalogue of sources was subtracted using AERES and the noise and background maps were measured again using BANE. The noise analysis was then performed as described above, to produce a background subtracted image and masked and source subtracted images, using the updated noise and background maps. In Fig. 4, we present the histograms of the pixel distributions for the 72–103 MHz images both before and after the improved background and noise estimates. Using the new background maps, the noise distribution becomes almost completely symmetric and follows the values measured by BANE.

The increasing resolution with the higher frequencies means only the lowest frequency band, 72–103 MHz, is significantly impacted by confusion, thus improved noise and background maps were only generated for the 72–103 MHz image and corresponding 7.68 MHz subband images. All noise and background maps are made available as part of the survey data release.

4 Final images

The 26 mosaics produced at the end of the combined multi-night mosaicking described in Section 3.5 are the combination of 28 nights of observing in 2020 and are Stokes I images across 72–231 MHz in five 30.72 MHz and 20 ‘subband’ 7.68 MHz bands as well as one deep 60 MHz band image across 170–231 MHz. There is decreasing sensitivity towards the edges of the mosaic, we therefore select a region with roughly consistent sensitivity covering 20 h40 m ≤ RA ≤ 6 h40 m, −90° ≤ Dec ≤ +30° (12,892-deg²) for this release. Postage stamps of all the images of this work are available on both the GLEAM-X website^d and AAO Data Central.

As described in Section 3.6, we calculate the noise and background maps for each mosaic using BANE with re-calculated background and RMS maps for the the lowest frequency band and corresponding subband images (i.e. 72–103 MHz). As with GLEAM-X DRI, we also performed 10 loops of 3-sigma-clipping to exclude the source-filled pixels in the background estimations. We present an example of 10 sq. deg of the 170–231 MHz wideband mosaic with its associated background and RMS noise maps and the same region in GLEAM ExGal (Hurley-Walker *et al.* 2017) in Fig. 5.

The RMS noise of the wideband 170–231 MHz image has a median of 1.5 mJy beam^{−1}, within the expectation of ∼1.2 mJy beam^{−1} calculated in GLEAM-X DRI. Likewise, in the 30 MHz images we find RMS values ranging from 7–2 mJy beam^{−1}, which

^d<https://www.mwatelescope.org/gleam-x>.

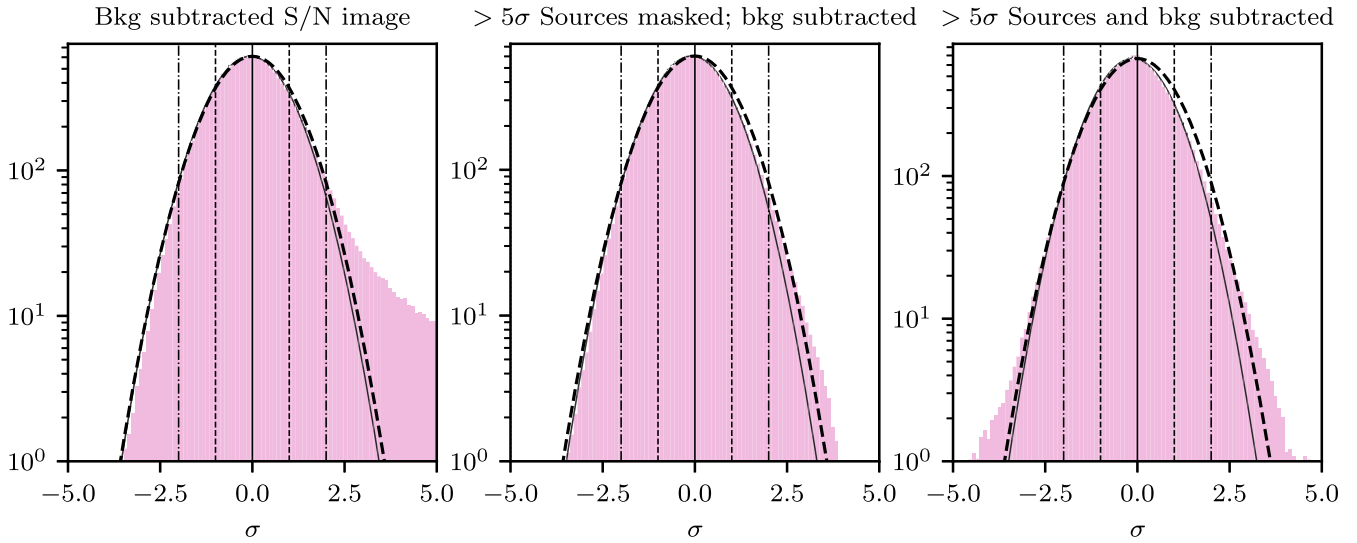


Figure 3. Pixel distribution for a 25 square degrees region of the wideband source finding image covering 170–231 MHz. BANE measure an RMS noise level in this region of $0.7 \text{ mJy beam}^{-1}$. The left most panel shows the distribution of the S/N of pixels in the image after the background has been subtracted and dividing by the RMS noise map. Sources that are detected at 5σ down to 0.2σ are then either masked using AERES (central panel) or subtracted (right panel). The black solid lines show Gaussian distributions with $\sigma = 1$ (as measured by BANE) and the black dashed Gaussian distribution is the fitted Gaussian to the pixel distribution. A similar distribution as measured by BANE to the pixel distribution indicates confusion is not impacting the effectiveness of BANE at measuring the background and RMS. The vertical solid lines indicate the mean values; dashed lines indicate $|S/N|=1\sigma$; and dash-dotted lines indicate $|S/N|=2\sigma$.

is also comparable to values reported in GLEAM-X DRI. While values are slightly higher than those reported in GLEAM-X DRI, we attribute this to the larger Declination coverage and bright A-team sources included in this data release. Large areas of this data release are found to have RMS noise levels $<1 \text{ mJy}$; we attribute the slight decrease in these areas to the improvements to the data reduction introduced in this release, for example, the sidelobe subtraction and self-calibration.

5 Compact source catalogue

As with GLEAM-X DRI, we present a source catalogue derived from the images in this work alongside with the mosaics. The details of the source detection and error derivation of this catalogue are described in full in GLEAM-X DRI, however, we summarise the detection strategy here. We use the algorithm AEGEAN to find sources in the most sensitive 170–231 MHz image that are $S/N > 4\sigma$. The positions for all sources in this catalogue are then used for ‘priorised’ fitting on the other images to measure the flux densities using the local PSF of the relevant narrow-band images. During the priorised fitting stage, if AEGEAN is unable to determine the error for a given parameter, it sets the error to a value of -1° , for these reason we use -1 as a flag value for the catalogue.

The catalogue is filtered to contain only sources within the defined region of this survey (i.e. $20 \text{ h}40 \text{ m} \leq \text{RA} \leq 6 \text{ h}40 \text{ m}$, $-90^\circ \leq \text{Dec} \leq +30^\circ$) with flux densities $\geq 5\sigma$, where σ denotes to local RMS noise. Simple spectral models are fit to all sources in the catalogue and sources that are fit well (described further in Section 5.2) have parameters reported in the final catalogue. The spectral modelling procedure is described further in Section 5.2.

The final catalogue, after filtering, consists of 624 866 radio sources detected over $12\,892 \text{ deg}^2$ with 562 302 sources with reported fits for either a power-law or curved spectrum. The increase in source density from GLEAM ExGal to this data release is likely due to a combination of increased resolution and sensitivity. A detailed analysis of source counts of this data release is presented in Venville et al. (2024). We present the main statistics of the compact source catalogue for this data release in Table 1 as well as a comparison to relevant surveys. The catalogue has 388 columns (described in Appendix C).

5.1 Comparison with DRI and GLEAM

Both GLEAM-X DRI and this data release use GLEAM as the basis for flux density calibration. Here we compare the flux densities measured in this work with GLEAM ExGal. A catalogue of sources that are compact in both catalogues ($S_{\text{int}}/S_{\text{peak}} < 2$), cross-match within a $15''$ radius, and have a confident power-law spectral index fit (reduced $\chi^2 < 1.93$, corresponding to a 99% confidence level) is used for all the following analysis.

We follow the same analysis outlined in GLEAM-X DRI and compare the ratio integrated flux densities as a function of SNR for both GLEAM-X DRI and GLEAM ExGal. The comparison of these ratios is presented in Fig. 6. As with GLEAM-X DRI, there is a trend towards 1.05 at higher SNR sources, however, as the effect is minimal we do not correct for it here. We advise an 8% error for the flux density scale of GLEAM-X DRI when comparing to other surveys, based on the 8% relative error of GLEAM for which our flux density scale is based.

We also compare the fitted spectral indices for components best fit by a power-law spectral model (α_{fitted}), presented in Fig. 7, and find no clear trends. The increase in SNR of GLEAM-X does result in consistently smaller error bars for α_{fitted} .

^cSee <https://github.com/PaulHancock/Aegean/wiki/AegeanErrors> for details.

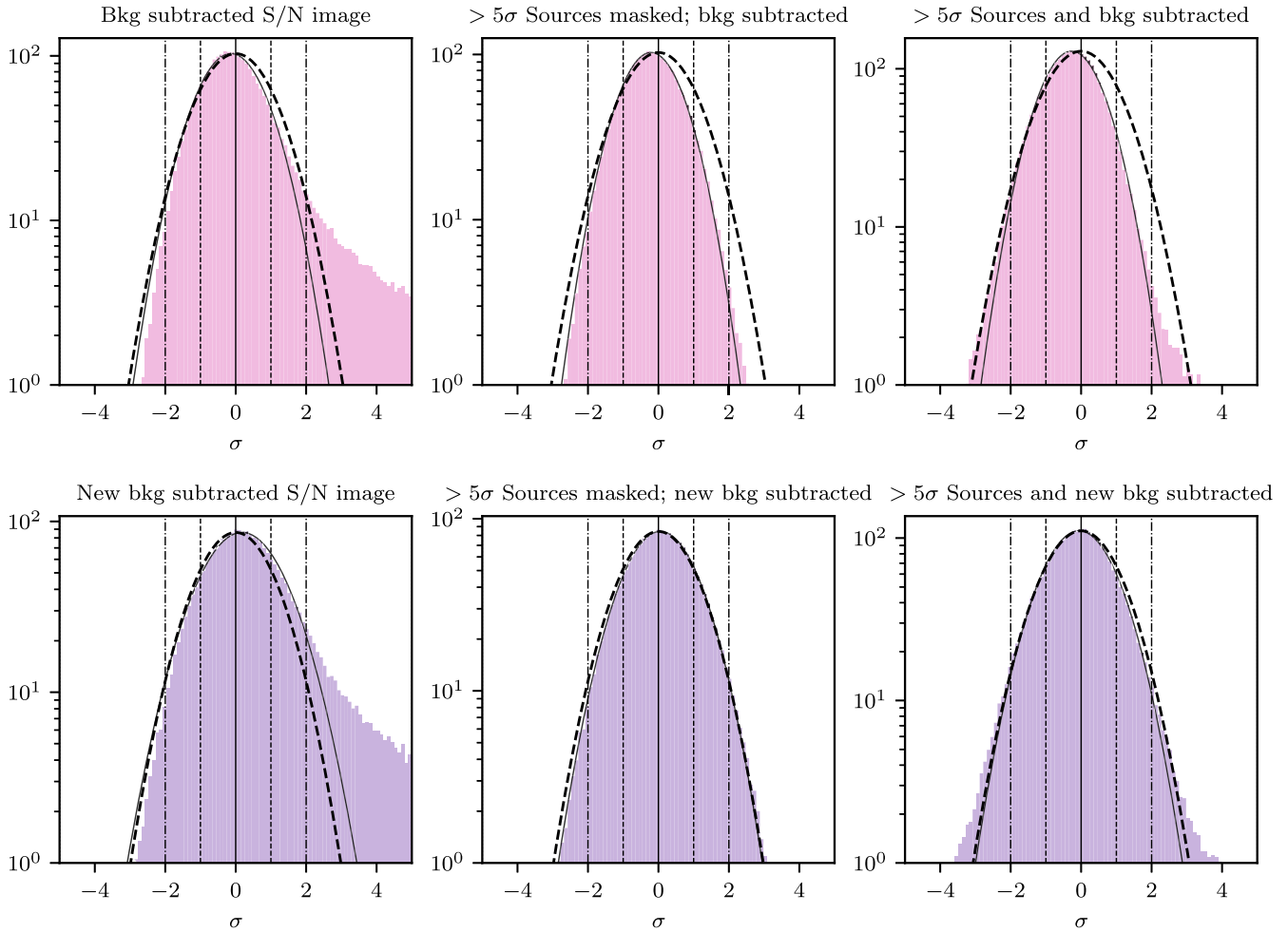


Figure 4. Pixel distribution for a 25 square degrees region of the lowest band image covering 72–103 MHz. The left, middle, and right panels are the same as described in Fig. 3. The top three panels use the initial background and RMS maps measured by BANE, while the bottom three panels use updated background and RMS maps measured by BANE after sources that were detected in the wideband source finding image are subtracted. The similarity of the solid line Gaussian distribution (measured by BANE) and the dashed line Gaussian distribution (fit to the pixel distribution) in the bottom three panels shows a dramatic improvement in the background and RMS estimation after sources are subtracted. Likewise, the difference in the distributions in the top three panels, indicates BANE does not accurately measure the background or RMS maps, likely due to confusion.

5.2 Spectral fitting

We fit two spectral models to the 20 narrow-band flux density measurements for all detected sources in the filtered compact source catalogue described in Section 5, we define the spectral index, α , as $S \propto \nu^\alpha$, such that a negative α describes a negative slope in logarithmic space.

Sources are first fit with a simple power-law model parameterised as:

$$S_\nu = S_{\nu_0} \left(\frac{\nu}{\nu_0} \right)^\alpha, \quad (1)$$

where S_{ν_0} , is the flux density in Jy at the reference frequency, ν_0 . The large fractional bandwidth of MWA allows for curvature to be detected and characterised within the MWA bandwidth. We therefore also fit a modified power-law model that parameterises the spectral curvature:

$$S_\nu = S_{\nu_0} \left(\frac{\nu}{\nu_0} \right)^\alpha \exp \left(q \ln \left(\frac{\nu}{\nu_0} \right)^2 \right), \quad (2)$$

where increasing $|q|$ describes increasing curvature, $q < 0$ corresponds to a concave curve and $q > 0$ corresponds to a convex curve (Duffy & Blundell 2012). Equation (2) has no physical motivation and is used as an initial identification of potential peaked-spectrum sources (PSS). A comprehensive catalogue of PSS in GLEAM-X will be given in a separate publication (Ross *et al.* in prep). In Fig. 8, shows example SEDs for three sources in this release: a source best fit with a typical, linear power-law, and two best fit with a curved power-laws.

Both the simple power-law and curved power-law models are fit using the SCIPY PYTHON module that applies a Levenberg–Marquardt non-linear least-squares regression algorithm (Virtanen *et al.* 2020). Narrow-band measurements that had a negative integrated flux density were excluded from fitting and fits are reported for sources if both of the following are true:

- there were at least 15 integrated flux density measurements;

Table 1. Survey properties and statistics GLEAM-X DR11 compared to both GLEAM-X DRI and the largest single data release from GLEAM ExGal. Values are given as the mean, \pm the standard deviation where appropriate. The statistics shown are derived from the wideband (170–231 MHz) image. The internal flux density scale error applies to all frequencies.

Property	GLEAM-X DR11	GLEAM ExGal	GLEAM-X DRI
Number of sources	624 866	307 456	78 967
Number of sources spectrally fit	562 302	254 453	71 320
Sky area	12 892 deg ²	24 402 deg ²	1 447 deg ²
Source density	48 deg ⁻²	13 deg ⁻²	55 deg ⁻²
RA astrometric offset	-7 ± 800 mas	$-4 \pm 16''$	$+14 \pm 700$ mas
Dec astrometric offset	$+4 \pm 800$ mas	$0.1 \pm 3.6''$	$+21 \pm 687$ mas
Internal flux density scale error	2 %	2 %	2 %
50% completeness	5.8 mJy	55 mJy	5.6 mJy
90% completeness	10.2 mJy	170 mJy	10 mJy
98% completeness	50 mJy	500 mJy	50 mJy
Reliability for $S_{\text{int}} \geq 7\sigma$	99.75%	99.8%	99.75%
Reliability for $S_{\text{int}} \geq 5\sigma$	98.7%	98.9%	98.7%
Image RMS noise	$1.5^{+1.5}_{-0.5}$ mJy beam ⁻¹	11.3 ± 7.3 mJy beam ⁻¹	1.27 ± 0.15 mJy beam ⁻¹
PSF major axis	$85 \pm 18''$	$152 \pm 25''$	$77 \pm 12''$
PSF minor axis	$64 \pm 8''$	$134 \pm 12''$	$61 \pm 6''$

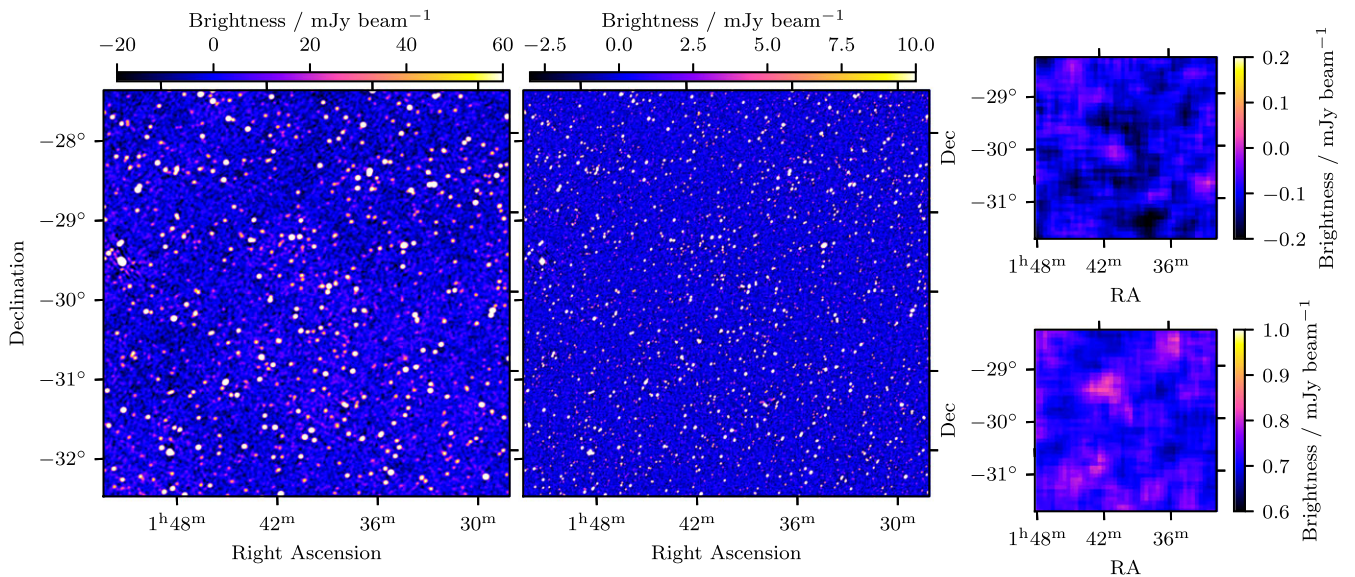


Figure 5. A ten square degree region in GLEAM ExGal and this work centred on 01 h40 m RA, -30° Dec. The left panel shows the region of the source finding 170–231 MHz mosaic in GLEAM ExGal, the central panel shows the same region in the source finding mosaic of this work, the top and bottom images in the right panel show the corresponding background and RMS noise of the GLEAM-X source finding image in the corresponding region. GLEAM ExGal contains 216 sources in this region, and the average RMS noise is 6 mJy beam^{-1} ; GLEAM-X contains 811 sources and the average RMS noise level is $0.8 \text{ mJy beam}^{-1}$.

- the χ^2 goodness-of-fit was above 99% likelihood confidence.

Similarly, a curved model is reported instead of the power-law model if the following criteria were all met:

- $q/\Delta q \geq 3$;
- $|q| > 0.2$;

- the reduced χ^2 for a power-law model was higher than the reduced χ^2 for a curved power-law model.

By adding the criteria $|q| > 0.2$, we avoid the potential for favouring a curved model over a power-law model for spectra that show only a small level of curvature (Callingham et al. 2017).

As with GLEAM-X DRI, the internal flux density scaling consistency of the catalogue is verified using the reduced χ^2 of the model fitting. We adopt 2% as the flux density scaling error as this

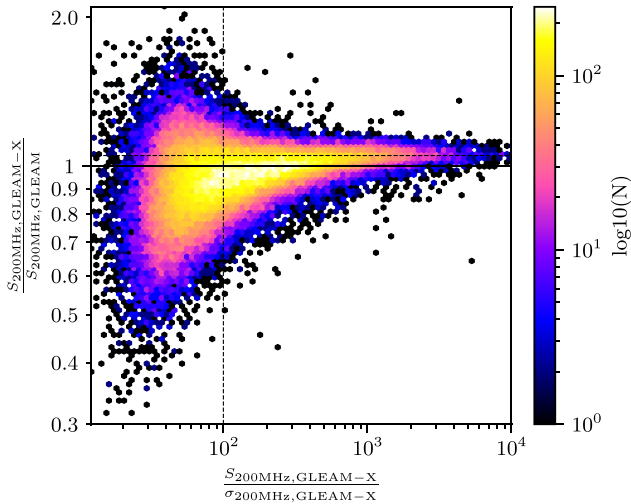


Figure 6. Ratio of the 200 MHz integrated flux density for compact sources matched in GLEAM-X DR11 and GLEAM as a function of signal-to-noise in GLEAM-X. The vertical dashed line is at a signal-to-noise of 100, corresponding to roughly 90% completeness in GLEAM. The horizontal solid line corresponds to a ratio of 1, and the horizontal dashed line corresponds to a ratio of 1.05, which fits the trend better. The same trend was detected in GLEAM-X DRI. Colour represented a density of points, error bars are omitted for clarity but are calculated as the quadrature sum of the measurement errors in both surveys.

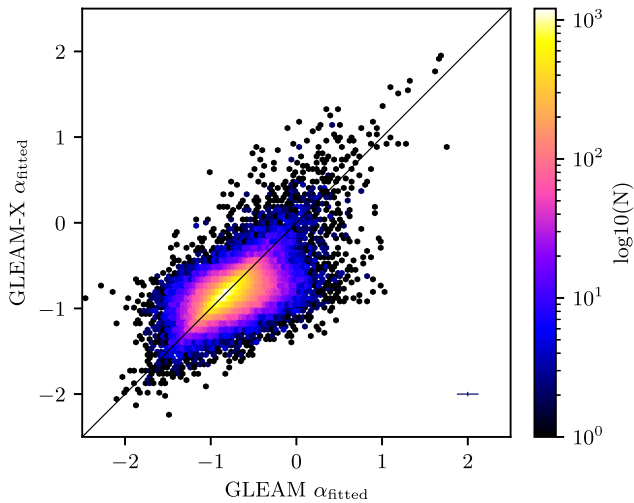


Figure 7. Spectral indices, α , based on a power-law spectral model, across the 7.68 MHz narrow bands for compact sources matched in both GLEAM and GLEAM-X. Colour corresponds to the density of points and an average of the error bars for fitting errors is shown at the bottom right, the fitting errors for GLEAM-X are significantly smaller due to the increase in signal-to-noise and thus confidence in spectral fitting for a given source. The diagonal line shows a 1:1 ratio of α .

produces a consistent median reduced χ^2 of unity as a function of SNR.

The distributions of α as a function of flux densities are presented in Fig. 9. The reported spectral indices of this data release are consistent with both GLEAM and GLEAM-X DRI, with a median α in the brightest flux density bin of -0.84 .

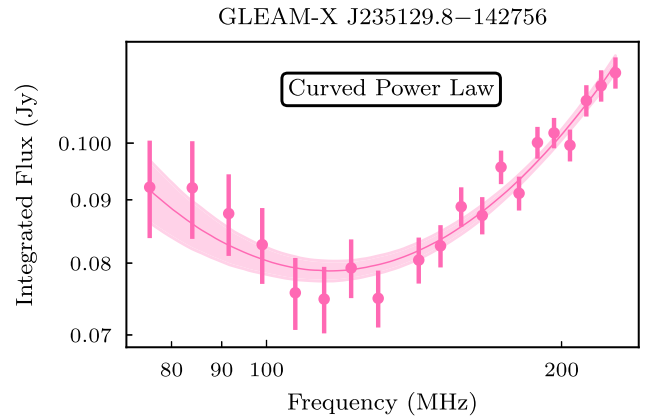
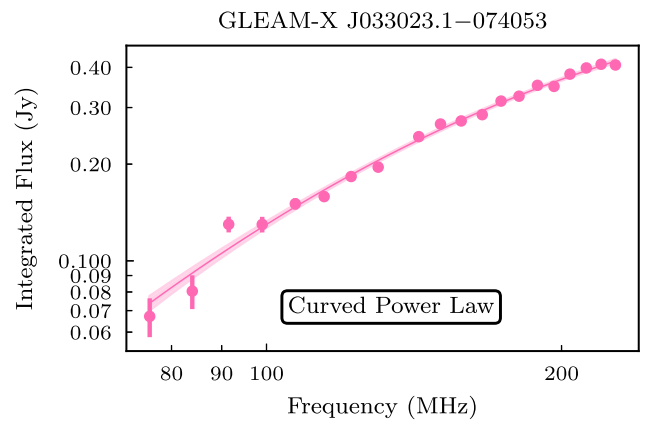
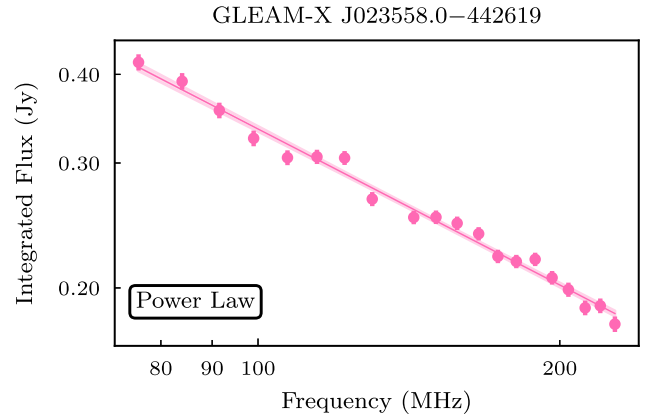


Figure 8. Example SEDs for 3 sources included in this data release. The title includes the source name as included in the catalogue, the inset includes the spectral model identified as the best fit model as outlined in Section 5.2. The optimised model and its 1σ confidence interval is overlaid as the pink line and shaded region of each source. The ‘Power Law’ and ‘Curved Power Law’ models are as defined by Equation 1 and Equation 2 respectively.

5.3 Astrometry

Following Hurley-Walker *et al.* (2017) and HW22, the astrometry is calculated using the wideband 170–231 MHz reference catalogue. Only GLEAM-X sources with a high SNR ($\geq 50\sigma$) were used to calculate offsets, corresponding to a total of 107 323 sources used for the astrometric analysis. A reference catalogue combining both SUMSS and NVSS was generated by filtering to

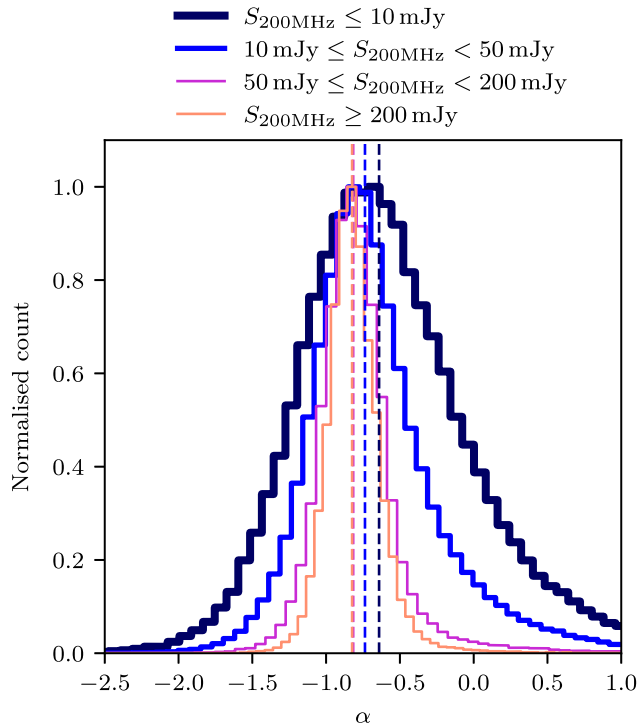


Figure 9. Distributions of the spectral index, α , for sources where the fit was successful, for various flux density bins. The dark navy line shows sources with $S_{200\text{MHz}} < 10$ mJy, the blue shows sources with $10 \leq S_{200\text{MHz}} < 50$ mJy, the purple line shows sources with $50 \leq S_{200\text{MHz}} < 200$ mJy, and the orange line shows sources with $S_{200\text{MHz}} \geq 200$ mJy. The dashed vertical lines of the same colours show the median values for each flux density cut: -0.58 , -0.77 , -0.84 , and -0.84 , respectively.

include only sparse (no internal cross matches within $3'$) and unresolved ($S_{\text{int}}/S_{\text{peak}} < 1.2$) sources. For astrometric calculations, the reported positions in the reference catalogue were assumed correct and offsets calculated relative to those positions. We find an average RA astrometric offset of -7 ± 800 mas and Declination astrometric offset of $+4 \pm 800$ mas, where errors on the astrometry are calculated from 1 standard deviation. In the final source catalogue presented in this work, we also report fitting errors on the positions for all sources, which typically are larger than the average astrometric offsets calculated here, we therefore do not correct for these offsets.

It is worth noting, during the processing of individual snapshot images, we conduct an astrometric offset correction based on positions reported in the same reference catalogue based on SUMSS and NVSS. For this reason, while we report sub-arcsecond astrometric offsets in the final mosaic, this is not necessarily a true representation of the astrometric properties of this catalogue. With more widefield low-frequency surveys of the Southern hemisphere being released, future analyses comparing the astrometric positions reported in this catalogue with an independent radio catalogue may be possible. We suggest care is taken when cross-matching this catalogue with other surveys, particularly at higher frequencies. We present the density distribution of the astrometric offsets in Fig. 10.

5.4 Completeness

We follow the same procedure as Hurley-Walker et al. (2017) and HW22, and use the wideband source finding mosaic to simulate

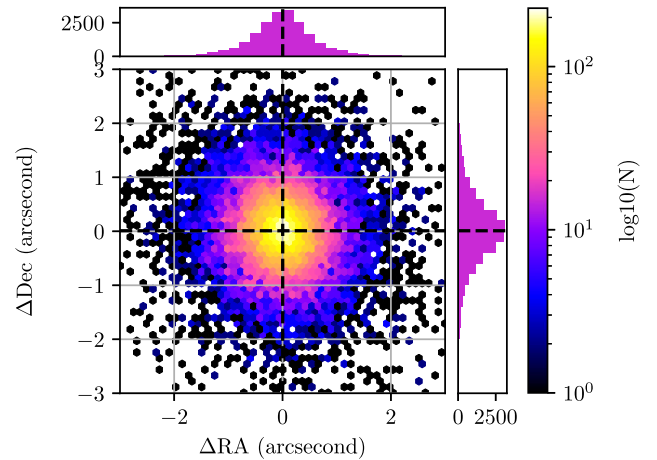


Figure 10. The astrometric offsets of 107,323 isolated, compact, $> 50\text{-}\sigma$ sources after cross-matching against the NVSS and SUMSS reference catalogue described in Section 5.3. Colour denotes density of points on a log scale. Vertical and horizontal dashed lines indicate the mean offset values in the RA and Dec directions, respectively. Similarly, the horizontal and vertical histograms highlight the counts of the astrometry offsets in each direction.

completeness of the source catalogue. We inject 130 000 simulated point sources evenly distributed across the region of this release, into the 170–231 MHz wideband mosaic. The simulated sources are injected with 26 realisations for different flux density increments spanning 10^{-3} to $10^{-0.5}$ Jy. Positions for all 90 000 simulated sources remain constant for each realisation, and to avoid confusion, simulated sources are separated by at least $5'$. The shape of the simulated sources is simulated based on the local major and minor axis of the PSF, and injected into the mosaic using AERES.

The same source finding procedure as described in Section 5 is performed on the mosaic with injected simulated sources for each of the 26 realisations. We then calculate the fraction of simulated sources that are recovered to estimate the completeness. For any simulated source that was detected but was near a real source, it was only included as ‘recovered’ if the recovered source position was closer to the simulated source rather than the real source.

In GLEAM-X DRI, the completeness was found to be around 50% at ~ 5.6 mJy and 90% at ~ 10 mJy. In this release, we find completeness that is overall consistent with expectations. The completeness for this work is estimated to be 50% at ~ 5.8 mJy and 90% at ~ 10.2 mJy. Fig. 11 presents the spatial distribution of fraction of simulated sources recovered. The smooth mosaicking of multiple drift scans in this release has produced a near uniform sensitivity and completeness across the region in this release, as expected. However, there is some dependence on RA due to bright A-team sources (most notably, Cygnus A and the Crab nebula) at $\text{RA} \approx 5$ h $\text{Dec} \approx +20$ d and $\text{RA} \approx 21$ h $\text{Dec} \approx +20$ d. There is a small Declination dependence for high and low Declinations. For high Declination ($\text{Dec} > 0$), observations are taken at low elevation, looking through a larger amount of ionosphere, and typically have more data flagged for poor data quality issues. Consequently, there is a roll off in completeness at high Declination ($\text{Dec} > 0$). However, the roll off in completeness at low Declination ($\text{Dec} < -80$) is more likely due to issues with recovering the simulated sources and differentiating from real sources due to the small sky area around the South Galactic Pole. Fig. 12 shows the fraction of simulated sources recovered as a function of the flux density at

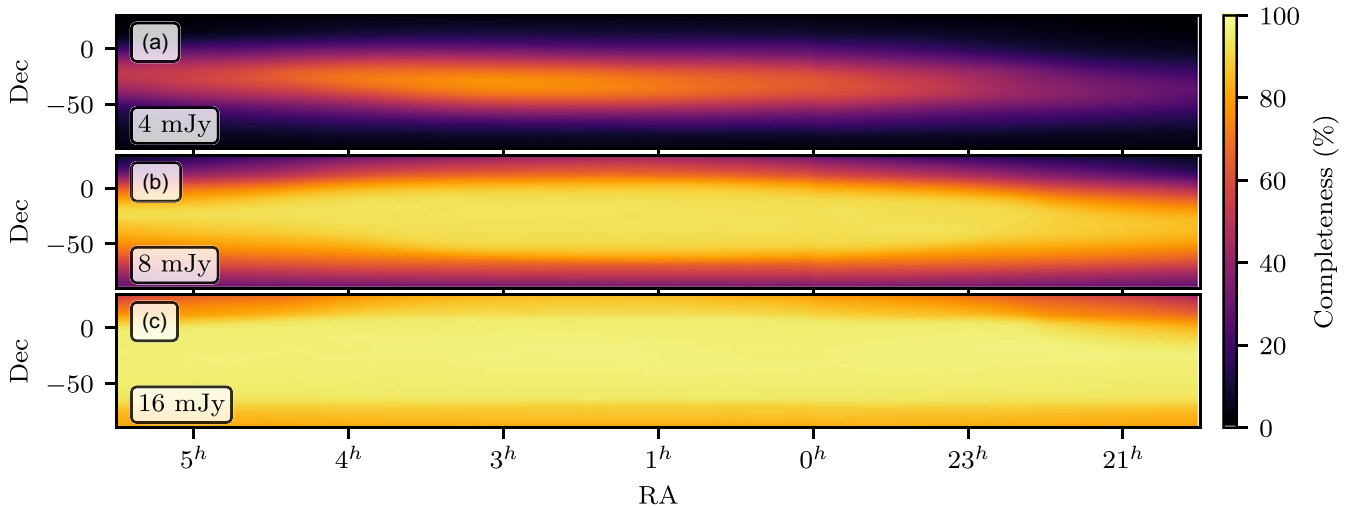


Figure 11. Completeness of the compact source catalogue of this work as a function of sky position for three representative cuts in source integrated flux density at 200 MHz. The three flux density cuts correspond to completeness levels of approximately 20%, 75%, and 95% shown in the subplots (a), (b), and (c) respectively.

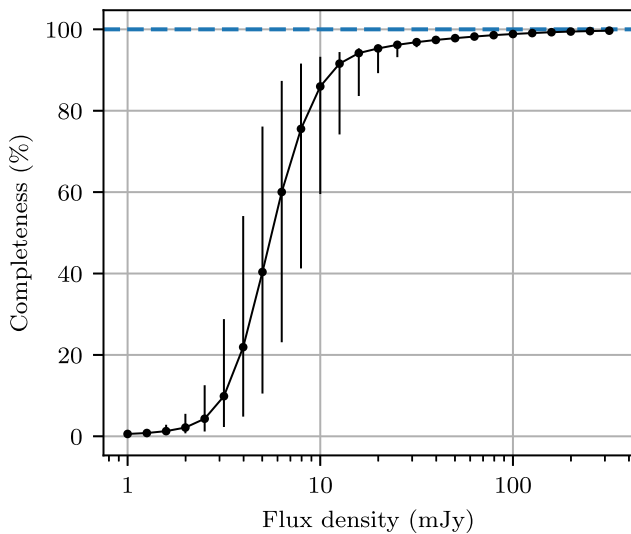


Figure 12. GLEAM-X DR11 completeness as a function of flux density in the wideband source finding mosaic covering 170–231 MHz. The RMS noise is roughly $1.5^{+1.5}_{-0.5}$ mJy beam⁻¹. Larger vertical bars compared to GLEAM-X DRI are due to the variations in completeness at high and low declinations and in regions near bright A-team sources.

200 MHz. The variations in the completeness results in the large error bars in Fig. 12.

5.5 Reliability and known issues

Following the reliability analysis of GLEAM-X DRI to check how many false detections may be present, we perform a source finding procedure to identify only negative peaks. Initially, we identify 10 305 negative detections, with 1 316 detections with $S_{\text{peak}} > 5\sigma$. As identified in GLEAM-X DRI, there is a tendency for artefacts around bright positive sources producing both negative and positive detections. The filter identified in GLEAM-X DRI was applied to exclude both the positive and negative detections that were near these bright sources. Furthermore, a second filter was applied to

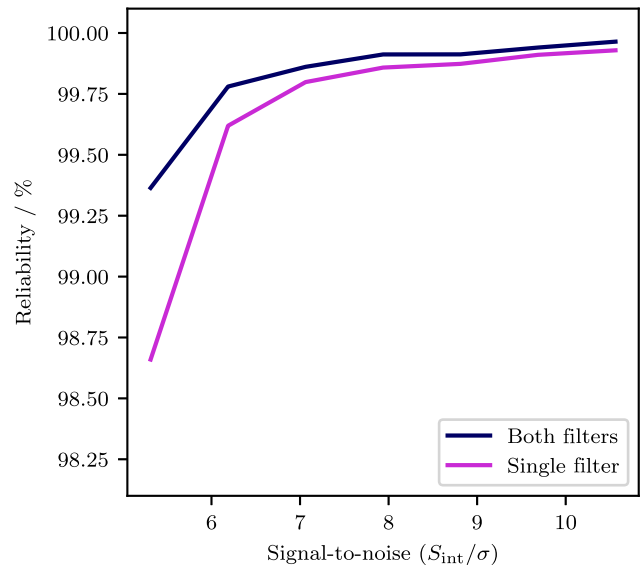


Figure 13. Estimates of the reliability of the catalogue as a function of signal-to-noise. The lower purple curve is a conservative estimate before filtering sources near bright positive sources. The upper dark navy line is derived after these sources have been filtered out. GLEAM ExGal has a reliability of $\sim 98.9\%$ – 99.8% at these signal-to-noise levels.

the negative sources to exclude any that were within $2'$ of a positive source, as these are likely a result of faint sidelobes of sources that were not properly cleaned.

We compare the negative and positive detections after applying the first filter and the second filter as a function of SNR. The reliability for each significance bin is presented in Fig. 13. For a conservative lower limit on the reliability for SNR at 5σ , we do not apply the second filter. We find the number of false detections to be 1.3% which falls quickly to under 1% at 7σ and a plateau for SNR $> 7\sigma$.

In this analysis, a region was identified as containing a higher density of high SNR negative detections relative to the rest

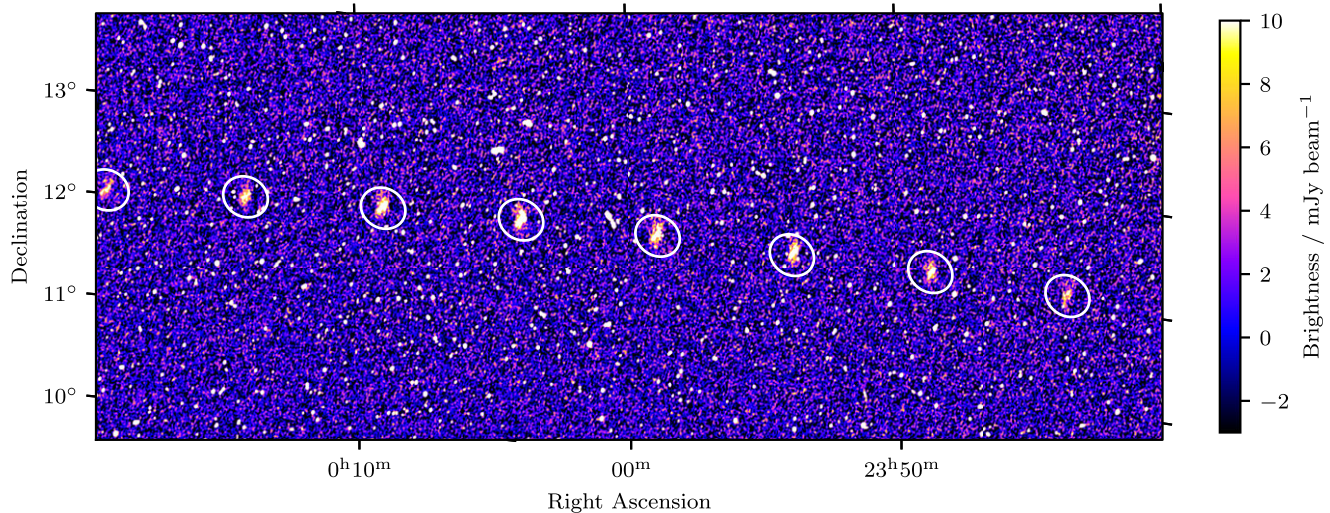


Figure 14. A cutout of the region with an identified repeating artefact due to bright contaminating sources in the sidelobe. The repeating artefact is highlighted by the white circles.

of the image. This region, covering roughly $23^{\text{h}} \leq \text{RA} \leq 1^{\text{h}}$, $+15^{\circ} \leq \text{Dec} \leq +30^{\circ}$, largely overlaps with a region excluded from GLEAM ExGal due to poor ionospheric conditions during observations. It is possible the combination of the low elevation pointing with sparse to no coverage of GLEAM used for calibration in this processing is contributing to the slightly lower reliability in this region. Furthermore, due to a bright source in the sidelobe (PKS 2365–61), for a subset of the observations taken for the +20 Declination drift scans, there is an artefact that appears as a bright source repeating at regular intervals across the high-frequency mosaics (170–200 MHz, 200–231 MHz, and the subbands for each wide images as well as the deep source finding mosaic 170–231 MHz). The sidelobe subtraction procedure, described in Section 3.2, reduces the flux density of this phantom source, but does not remove the artefact entirely. The repeating artefact in this region is presented in Fig. 14.

6 Summary and outlook

In this work, we present the second data release of the GLEAM-X survey, comprising of images and an extragalactic source catalogue. This data release covers 12 892-deg^2 covering $20^{\text{h}} 40^{\text{m}} \leq \text{RA} \leq 6^{\text{h}} 40^{\text{m}}$, $-90^{\circ} \leq \text{Dec} \leq +30^{\circ}$ over 72–231 MHz in the form of 26 mosaics with bandwidths 60, 30 and 8 MHz. These mosaics have typical RMS noise levels ranging from $\approx 1 \text{ mJy beam}^{-1}$ in the 60 MHz bandwidth mosaic used for initial source finding to $\approx 10 \text{ mJy beam}^{-1}$ in the 8 MHz mosaic at the lowest frequency, 72–80 MHz. The RMS noise levels of this region are an order of magnitude lower than that reported in GLEAM ExGal (Hurley-Walker et al. 2017) and within expectations for the overall survey as reported by HW22.

We also present a catalogue of 624 866 components, 562 302 of which are well fit by either a power-law or curved power-law spectral model. This results in a source density of 48 deg^{-2} . We estimate this catalogue is 98% complete at 50 mJy for the entire region with near uniform sensitivity and completeness across the region covered in this release, as expected. We estimate a reliability of 98.7% at a 5σ level. We identify 18 869 sources as being

better fit by a curved power-law, suggesting an order of magnitude increase in the PSS sources from those identified using GLEAM (Callingham et al. 2017), and probing a population of fainter PSS. A comprehensive catalogue of PSS and population analysis will be described in an upcoming paper by Ross et al. (in preparation).

The data reduction of this release largely follows that of GLEAM-X DRI (Hurley-Walker et al. 2022a), but with some noticeable improvements that are now incorporated to future GLEAM-X processing. The subtraction of a model of sensitive sidelobes for observations taken at low elevation reduced the occurrence and/or S/N of alias sources appearing in the main lobe. The use of self-calibration for fields with bright and complex sources in the main lobe or sensitive sidelobes was also introduced and resulted in an improvement in the RMS noise levels of snapshot images. Lastly, a stricter quality assessment of blurring due to the ionosphere resulted in fewer poor quality snapshot observations being included in the final mosaics of this release, resulting in an overall improvement in the mosaic quality.

The uniform and high source density provided by this data release has enabled a study of the source count statistics and a measurement of the angular correlation function, which are presented by Venville et al. (2024). A search for transients on seconds to hours timescales has also been carried out and will be described in full by Horvath et al. (in preparation).

We aim to release the remainder of GLEAM-X via a series of releases. The POLarised GLEAM-X Survey (POGS-X) will be described fully by Zhang et al. (in prep); a Galactic plane release combining both GLEAM and GLEAM-X observations using joint deconvolution, which will be described in Mantovanini et al. (in prep); finally, we aim to produce a contiguous all-sky coverage and release the remainder of GLEAM-X (Ross et al. in preparation).

The images and source catalogue of the GLEAM-X DRII data release are publicly available at AAO Data Central (<https://datacentral.org.au/services/cutout/>).

Acknowledgements. NHW is supported by an Australian Research Council Future Fellowship (project number FT190100231) funded by the Australian Government. This scientific work uses data obtained from Inyarrimanha Ilgari

Bundara/the Murchison Radio-astronomy Observatory. We acknowledge the Wajarri Yamaji People as the Traditional Owners and native title holders of the Observatory site. Establishment of CSIRO's Murchison Radio-astronomy Observatory is an initiative of the Australian Government, with support from the Government of Western Australia and the Science and Industry Endowment Fund. Support for the operation of the MWA is provided by the Australian Government (NCRIS), under a contract to Curtin University administered by Astronomy Australia Limited. This work was supported by resources provided by the Pawsey Supercomputing Research Centre with funding from the Australian Government and the Government of Western Australia. Access to Pawsey Data Storage Services is governed by a Data Storage and Management Policy (DSMP). ASVO has received funding from the Australian Commonwealth Government through the National eResearch Collaboration Tools and Resources (NeCTAR) Project, the Australian National Data Service (ANDS), and the National Collaborative Research Infrastructure Strategy. This paper makes use of services or code that have been provided by AAO Data Central (datacentral.org.au). This research has made use of NASA's Astrophysics Data System Bibliographic Services. The following software was used in this work: AOFLAGGER and COTTER (Offringa, van de Gronde, & Roerdink 2012); WSCLEAN (Offringa et al. 2014; Offringa & Smirnov 2017); AEGEAN (Hancock et al. 2018); MIRIAD (Sault, Teuben, & Wright 1995) NUMPY (Dubois, Hinsen, & Hugunin 1996; Harris et al. 2020); ASTROPY (Astropy Collaboration et al. 2013); SCIPLY (Oliphant 2007); MATPLOTLIB (Hunter 2007). We also made extensive use of the visualisation and analysis packages DS9^f and Topcat (Taylor 2005). This work was compiled in the very useful online L^AT_EX editor Overleaf.

Data availability. The catalogue associated with this paper is available at CDS via anonymous ftp to cdsarc.u-strasbg.fr (130.79.128.5) or via <https://cdsarc.cds.unistra.fr/viz-bin/cat/VIII/113>. Mosaics associated with this data release are made available via AAO Data Central and SkyView.

References

- Adams, E. A. K., et al. 2022, *A&A* 667, A38
 Astropy Collaboration et al. 2013, *A&A* 558, A33
 Beardsley, A. P., et al. 2019, *PASA*, 36, e050
 Bertin, E., Mellier, Y., Radovich, M., Missonnier, G., Didelon, P., & Morin, B. 2002, in *Astronomical Society of the Pacific Conference Series*, Vol. 281, *Astronomical Data Analysis Software and Systems XI*, ed. D. A. Bohlender, D. Durand, & T. H. Handley, 228
 Best, P. N., et al. 2023, *MNRAS*, 523, 1729
 Briggs, D. S. 1995, in *American Astronomical Society Meeting Abstracts*, 112.02
 Callingham, J. R., et al. 2017, *ApJ*, 836, 174
 Condon, J. J., Cotton, W. D., Greisen, E. W., Yin, Q. F., Perley, R. A., Taylor, G. B., & Broderick, J. J. 1998, *AJ*, 115, 1693
 de Gasperin, F., et al. 2021, *A&A*, 648, A104
 de Gasperin, F., et al. 2023, *A&A*, 673, A165
 Deka, P. P., et al. 2023, arXiv e-prints, p. [arXiv:2308.12347](https://arxiv.org/abs/2308.12347)
 Dubois, P. F., Hinsen, K., & Hugunin, J. 1996, *CPhC*, 10, 262
 Duchesne, S. W., Johnston-Hollitt, M., Zhu, Z., Wayth, R. B., & Line, J. L. B. 2020, *PASA*, 37, e037
 Duchesne, S. W., et al. 2023, *PASA*, 40, e034
 Duffy, P., & Blundell, K. M. 2012, *MNRAS*, 421, 108
 Franzen, T. M. O., Hurley-Walker, N., White, S. V., Hancock, P. J., Seymour, N., Kapińska, A. D., Staveley-Smith, L., & Wayth, R. B. 2021, *PASA*, 38, e014
 Franzen, T. M. O., Vernstrom, T., Jackson, C. A., Hurley-Walker, N., Ekers, R. D., Heald, G., Seymour, N., & White, S. V. 2019, *PASA*, 36, e004
 Hale, C. L., et al. 2024, *MNRAS*, 527, 6540
 Hancock, P. J., Murphy, T., Gaensler, B. M., Hopkins, A., & Curran, J. R. 2012, *MNRAS*, 422, 1812
 Hancock, P. J., Trott, C. M., & Hurley-Walker, N. 2018, *PASA*, 35, e011
 Harris, C. R., et al. 2020, *Natur*, 585, 357

- Heywood, I., et al. 2022, *MNRAS*, 509, 2150
 Hunter, J. D. 2007, *CSE*, 9, 90
 Hurley-Walker, N., et al. 2017, *MNRAS*, 464, 1146
 Hurley-Walker, N., et al. 2022a, *PASA*, 39, e035
 Hurley-Walker, N., et al. 2022b, *Natur*, 601, 526
 Kurtzer, G. M., Sochat, V., & Bauer, M. W. 2017, *PLoS ONE*, 12, e0177459
 Lacy, M., et al. 2020, *PASP*, 132, 035001
 Mauch, T., Murphy, T., Buttery, H. J., Curran, J., Hunstead, R. W., Piestrzynski, B., Robertson, J. G., & Sadler, E. M. 2003, *MNRAS*, 342, 1117
 McConnell, D., et al. 2020, *PASA*, 37, e048
 Morabito, L. K., et al. 2022, *A&A*, 658, A1
 Morgan, J. S., Chhetri, R., & Ekers, R. 2022, *PASA*, 39, e063
 Morgan, J., McCauley, P. I., Waszewski, A., Ekers, R., & Chhetri, R. 2023, *SpWea*, 21, e2022SW003396
 Offringa, A. R., & Smirnov, O. 2017, *MNRAS*, 471, 301
 Offringa, A. R., van de Gronde, J. J., & Roerdink, J. B. T. M. 2012, *A&A*, 539, A95
 Offringa, A. R., et al. 2014, *MNRAS*, 444, 606
 Offringa, A. R., et al. 2016, *MNRAS*, 458, 1057
 Oliphant, T. E. 2007, *CSE*, 9, 10
 Riseley, C. J., et al. 2018, *PASA*, 35, e043
 Riseley, C. J., et al. 2020, *PASA*, 37, e029
 Ross, K., Hurley-Walker, N., Seymour, N., Callingham, J. R., Galvin, T. J., & Johnston-Hollitt, M. 2022, *MNRAS*, 512, 5358
 Sault, R. J., Teuben, P. J., & Wright, M. C. H. 1995, in *ASP Conference Series*, Vol. 77, *Astronomical Data Analysis Software and Systems IV*, ed. R. A. Shaw, H. E. Payne, & J. J. E. Hayes, 433 ([arXiv:astro-ph/0612759](https://arxiv.org/abs/astro-ph/0612759))
 Shimwell, T. W., et al. 2017, *A&A*, 598, A104
 Shimwell, T. W., et al. 2022, *A&A*, 659, A1
 Taylor, M. B. 2005, in *ASP Conference Series*, Vol. 347, *Astronomical Data Analysis Software and Systems XIV*, ed. P. Shopbell, M. Britton, & R. Ebert, 29
 Thomson, A. J. M., et al. 2023, *PASA*, 40, e040
 Tingay, S. J., et al. 2013, *PASA*, 30, 7
 van der Tol, S., Jeffs, B. D., & van der Veen, A. J. 2007, *IEEE TSP*, 55, 4497
 van Haarlem, M. P., et al. 2013, *A&A*, 556, A2
 Venville, B., et al. 2024, arXiv e-prints, p. [arXiv:2407.12394](https://arxiv.org/abs/2407.12394)
 Vernstrom, T., Heald, G., Vazza, F., Galvin, T. J., West, J. L., Locatelli, N., Fornengo, N., & Pinetti, E. 2021, *MNRAS*, 505, 4178
 Virtanen, P., et al. 2020, *NM*, 17, 261
 Wayth, R. B., et al. 2015, *PASA*, 32, e025
 Wayth, R. B., et al. 2018, *PASA*, 35, e033
 White, S. V., et al. 2020a, *PASA*, 37, e017
 White, S. V., et al. 2020b, *PASA*, 37, e018

A Observations

Table A1. GLEAM-X DR11 observing summary of the 28 nights published in this work. The HA and Dec are fixed to the locations shown and the sky drifts past for the observing time shown. Observations typically start just after sunset and stop just before sunrise. Nights identified as having high ionospheric activity by Hurley-Walker et al. (2022a) are marked with a “*”.

Date	HA	Dec (°)	Observing time (hours)
2020-09-28*	−1	−71	9.8
2020-09-29	−1	−54	9.3
2020-09-30*	−1	−39	8.2
2020-10-01*	−1	−25	7.8
2020-10-02	−1	−11	7.9
2020-10-03	−1	+2	9.8
2020-10-04*	−1	+19	9.8
2020-10-05	0	−72	9.8
2020-10-06	0	−55	9.8

^f<http://ds9.si.edu/site/Home.html>.

Table A1. Continued

Date	HA	Dec (°)	Observing time (hours)
2020-10-07	0	−40	9.8
2020-10-08	0	−26	9.8
2020-10-09	0	−12	9.6
2020-10-10*	0	+1	8.8
2020-10-11	0	+18	9.8
2020-10-12	0	−72	8.6
2020-10-13	0	−55	8.4
2020-10-14	0	−40	5.6
2020-10-15	0	−26	9.1
2020-10-16	0	−12	9.0
2020-10-17*	0	+1	9.8
2020-10-18	0	+18	9.7
2020-10-19	+1	−71	9.5
2020-10-20	+1	−54	9.5
2020-10-21	+1	−39	9.5
2020-10-22	+1	−25	8.2
2020-10-23	+1	−11	9.5
2020-10-24*	+1	+2	9.5
2020-10-25	+1	+19	8.0
		Total:	253.9

B Noise Analysis

Given the large sky coverage of this data release, we repeat the noise analysis outlined in Section 3.6 for a region of lower quality and lower elevations for the MWA. In Fig. B1, we present the pixel distributions for a 25 square degrees region in the lowest wideband image covering 72–103 MHz centred at RA $2^{\text{h}}30^{\text{m}}$ Dec+ $15^{\circ}00'$. The lower elevations of this region can elongate the PSF, however, in GLEAM-X DRI, we outlined a strategy for ensuring the PSF is well defined over the entire region. Consequently, we find the well defined PSF, even in areas of low elevation, ensures we are able to accurately detect and subtract sources from the lowest band in order to reduce the impact of confusion. Comparing the distributions for the optimal scenario (presented in Fig. 4), to that of the ‘worst case’ scenario in Fig. B1, we can see the strategy for estimating the noise and RMS maps is still appropriate and we are not significantly impacted by confusion.

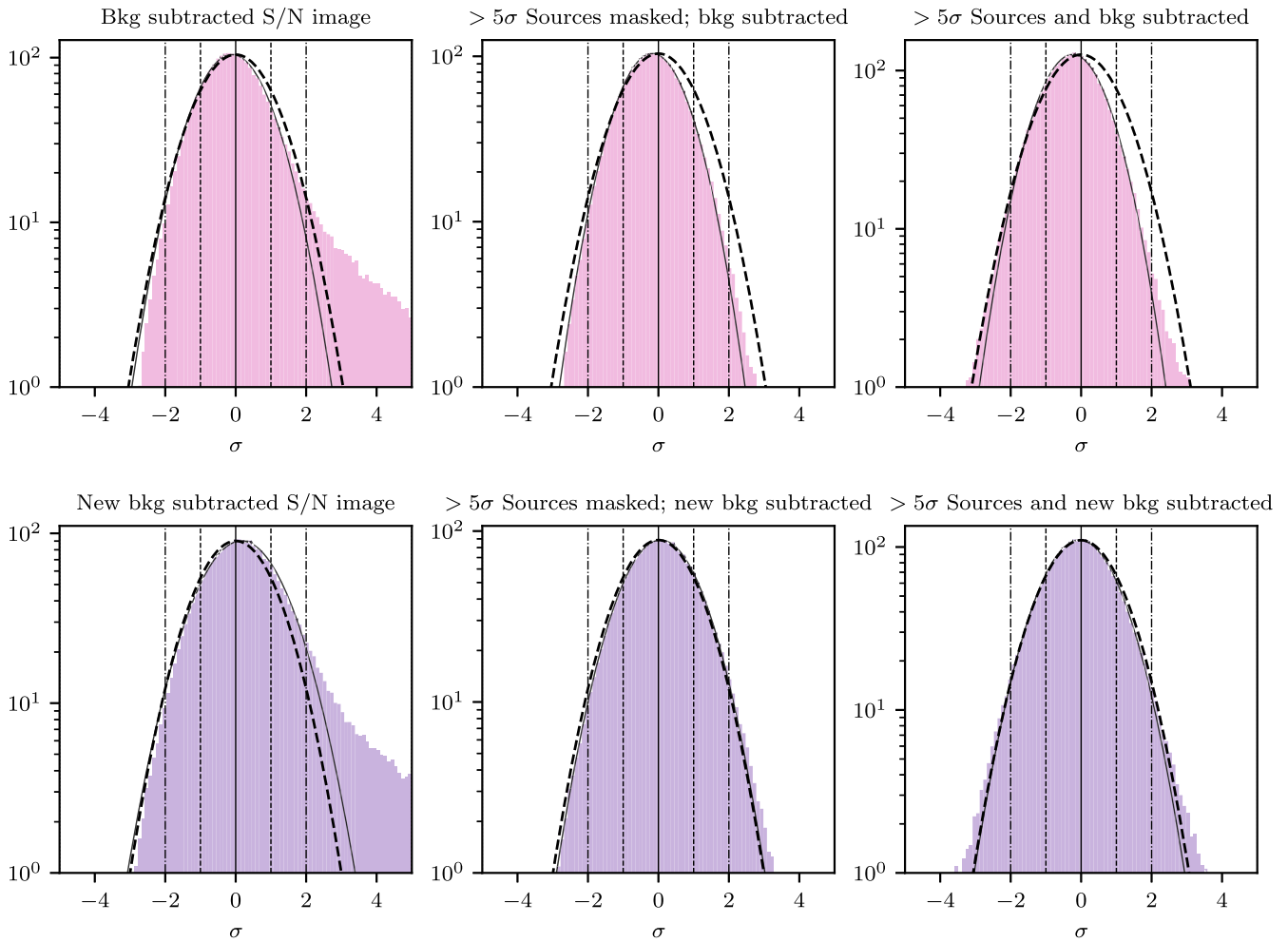


Figure B1. Pixel distribution for a 25 square degrees region of the lowest band image covering 72–103 MHz centred at RA $2^{\text{h}}30^{\text{m}}$ Dec $+15^{\circ}00'$. All six panels are the same as described in Fig. 4: The top three panels use the initial background and RMS maps measured by BANE, while the bottom three panels use updated background and RMS maps measured by BANE after sources that were detected in the wideband source finding image are subtracted. The similarity of the solid line Gaussian distribution (measured by BANE) and the dashed line Gaussian distribution (fit to the pixel distribution) in the bottom three panels shows a dramatic improvement in the background and RMS estimation after sources are subtracted. Likewise, the difference in the distributions in the top three panels, indicates BANE does not accurately measure the background or RMS maps, likely due to confusion.

C Catalogue Column Names

Table A2. Column numbers, names, and units for the catalogue. Source names follow International Astronomical Union naming conventions for coordinate-based naming. Background and RMS measurements were performed by BANE (Section 4); PSF measurements were performed using in-house software as described in Hurley-Walker et al. (2022a); the fitted spectral index parameters were derived as described in Section 5.2; all other measurements were made using AEGEAN. AEGEAN incorporates a constrained fitting algorithm. Shape parameters with an error of -1 indicate that the reported value is equal to either the upper or lower fitting constraint. The columns with the subscript ‘wide’ are derived from the 200 MHz wideband image. Subsequently, the subscript indicates the central frequency of the measurement, in MHz. These subband measurements are made using the prioritised fitting mode of Aegean, where the position and shape of the source are determined from the wideband image, and only the flux density is fitted (see Section 5). Note therefore that some columns in the prioritised fit do not have error bars, because they are linearly propagated from the wideband image values (e.g. major axis a).

Number	Name	Unit	Description
1	Name	hh:mm:ss+dd:mm:ss	International Astronomical Union name
2	background_wide	Jy beam ⁻¹	Background in wideband image
3	local_rms_wide	Jy beam ⁻¹	Local RMS in wideband image
4	ra_str	hh:mm:ss	Right ascension
5	dec_str	dd:mm:ss	Declination
6	RAJ2000	°	Right ascension
7	err_RAJ2000	°	Error on RA
8	DEJ2000	°	Declination
9	err_DEJ2000	°	Error on Dec
10	peak_flux_wide	Jy beam ⁻¹	Peak flux density in wideband image
11	err_peak_flux_wide	Jy beam ⁻¹	Fitting error on peak flux density in wideband image
12	int_flux_wide	Jy	Integrated flux density in wideband image
13	err_int_flux_wide	Jy	Error on integrated flux density in wideband image
14	a_wide	//	Major axis of source in wideband image
15	err_a_wide	//	Error on major axis of source in wideband image
16	b_wide	//	Minor axis of source in wideband image
17	err_b_wide	//	Error on minor axis of source in wideband image
18	pa_wide	°	Position angle of source in wideband image
19	err_pa_wide	°	Error on position angle of source in wideband image
20	residual_mean_wide	Jy beam ⁻¹	Mean of residual after source fitting in wideband image
21	residual_std_wide	Jy beam ⁻¹	Standard deviation of residual after source fitting
22	err_abs_flux_pct	%	Percent error in absolute flux scale - all frequencies
23	err_fit_flux_pct	%	Percent error on internal flux scale - all frequencies
24	psf_a_wide	//	Major axis of PSF at location of source in wideband image
25	psf_b_wide	//	Minor axis of PSF at location of source in wideband image
26	psf_pa_wide	°	Position angle of PSF at location of source in wideband image
27	background_076	Jy beam ⁻¹	Background at 76 MHz
28	local_rms_076	Jy beam ⁻¹	Local RMS at 76 MHz
29	peak_flux_076	Jy beam ⁻¹	Peak flux density at 76 MHz
30	err_peak_flux_076	Jy beam ⁻¹	Fitting error on peak flux density at 76 MHz
31	int_flux_076	Jy	Integrated flux density at 76 MHz
32	err_int_flux_076	Jy	Fitting error on integrated flux density at 76 MHz
33	a_076	//	Major axis of source at 76 MHz
34	b_076	//	Minor axis of source at 76 MHz
35	pa_076	°	Position angle of source at 76 MHz
36	residual_mean_076	Jy beam ⁻¹	Mean of residual after source fitting at 76 MHz
37	residual_std_076	Jy beam ⁻¹	Standard deviation of residual after source fitting at 76 MHz

Table A2. Continued

Number	Name	Unit	Description
38	psf_a_076	//	Major axis of PSF at location of source at 76 MHz
39	psf_b_076	//	Minor axis of PSF at location of source at 76 MHz
40	psf_pa_076	°	Position angle of PSF at location of source at 76 MHz
41	background_084	Jy beam ⁻¹	Background at 84 MHz
42	local_rms_084	Jy beam ⁻¹	Local RMS at 84 MHz
43	peak_flux_084	Jy beam ⁻¹	Peak flux density at 84 MHz
44	err_peak_flux_084	Jy beam ⁻¹	Fitting error on peak flux density at 84 MHz
45	int_flux_084	Jy	Integrated flux density at 84 MHz
46	err_int_flux_084	Jy	Fitting error on integrated flux density at 84 MHz
47	a_084	//	Major axis of source at 84 MHz
48	b_084	//	Minor axis of source at 84 MHz
49	pa_084	°	Position angle of source at 84 MHz
50	residual_mean_084	Jy beam ⁻¹	Mean of residual after source fitting at 84 MHz
51	residual_std_084	Jy beam ⁻¹	Standard deviation of residual after source fitting at 84 MHz
52	psf_a_084	//	Major axis of PSF at location of source at 84 MHz
53	psf_b_084	//	Minor axis of PSF at location of source at 84 MHz
54	psf_pa_084	°	Position angle of PSF at location of source at 84 MHz
55	background_092	Jy beam ⁻¹	Background at 92 MHz
56	local_rms_092	Jy beam ⁻¹	Local RMS at 92 MHz
57	peak_flux_092	Jy beam ⁻¹	Peak flux density at 92 MHz
58	err_peak_flux_092	Jy beam ⁻¹	Fitting error on peak flux density at 92 MHz
59	int_flux_092	Jy	Integrated flux density at 92 MHz
60	err_int_flux_092	Jy	Fitting error on integrated flux density at 92 MHz
61	a_092	//	Major axis of source at 92 MHz
62	b_092	//	Minor axis of source at 92 MHz
63	pa_092	°	Position angle of source at 92 MHz
64	residual_mean_092	Jy beam ⁻¹	Mean of residual after source fitting at 92 MHz
65	residual_std_092	Jy beam ⁻¹	Standard deviation of residual after source fitting at 92 MHz
66	psf_a_092	//	Major axis of PSF at location of source at 92 MHz
67	psf_b_092	//	Minor axis of PSF at location of source at 92 MHz
68	psf_pa_092	°	Position angle of PSF at location of source at 92 MHz
69	background_099	Jy beam ⁻¹	Background at 99 MHz
70	local_rms_099	Jy beam ⁻¹	Local RMS at 99 MHz
71	peak_flux_099	Jy beam ⁻¹	Peak flux density at 99 MHz
72	err_peak_flux_099	Jy beam ⁻¹	Fitting error on peak flux density at 99 MHz
73	int_flux_099	Jy	Integrated flux density at 99 MHz
74	err_int_flux_099	Jy	Fitting error on integrated flux density at 99 MHz
75	a_099	//	Major axis of source at 99 MHz
76	b_099	//	Minor axis of source at 99 MHz
77	pa_099	°	Position angle of source at 99 MHz
78	residual_mean_099	Jy beam ⁻¹	Mean of residual after source fitting at 99 MHz
79	residual_std_099	Jy beam ⁻¹	Standard deviation of residual after source fitting at 99 MHz
80	psf_a_099	//	Major axis of PSF at location of source at 99 MHz
81	psf_b_099	//	Minor axis of PSF at location of source at 99 MHz
82	psf_pa_099	°	Position angle of PSF at location of source at 99 MHz
83	background_107	Jy beam ⁻¹	Background at 107 MHz

Table A2. Continued

Number	Name	Unit	Description
84	local_rms_107	Jy beam ⁻¹	Local RMS at 107 MHz
85	peak_flux_107	Jy beam ⁻¹	Peak flux density at 107 MHz
86	err_peak_flux_107	Jy beam ⁻¹	Fitting error on peak flux density at 107 MHz
87	int_flux_107	Jy	Integrated flux density at 107 MHz
88	err_int_flux_107	Jy	Fitting error on integrated flux density at 107 MHz
89	a_107	//	Major axis of source at 107 MHz
90	b_107	//	Minor axis of source at 107 MHz
91	pa_107	°	Position angle of source at 107 MHz
92	residual_mean_107	Jy beam ⁻¹	Mean of residual after source fitting at 107 MHz
93	residual_std_107	Jy beam ⁻¹	Standard deviation of residual after source fitting at 107 MHz
94	psf_a_107	//	Major axis of PSF at location of source at 107 MHz
95	psf_b_107	//	Minor axis of PSF at location of source at 107 MHz
96	psf_pa_107	°	Position angle of PSF at location of source at 107 MHz
97	background_115	Jy beam ⁻¹	Background at 115 MHz
98	local_rms_115	Jy beam ⁻¹	Local RMS at 115 MHz
99	peak_flux_115	Jy beam ⁻¹	Peak flux density at 115 MHz
100	err_peak_flux_115	Jy beam ⁻¹	Fitting error on peak flux density at 115 MHz
101	int_flux_115	Jy	Integrated flux density at 115 MHz
102	err_int_flux_115	Jy	Fitting error on integrated flux density at 115 MHz
103	a_115	//	Major axis of source at 115 MHz
104	b_115	//	Minor axis of source at 115 MHz
105	pa_115	°	Position angle of source at 115 MHz
106	residual_mean_115	Jy beam ⁻¹	Mean of residual after source fitting at 115 MHz
107	residual_std_115	Jy beam ⁻¹	Standard deviation of residual after source fitting at 115 MHz
108	psf_a_115	//	Major axis of PSF at location of source at 115 MHz
109	psf_b_115	//	Minor axis of PSF at location of source at 115 MHz
110	psf_pa_115	°	Position angle of PSF at location of source at 115 MHz
111	background_122	Jy beam ⁻¹	Background at 122 MHz
112	local_rms_122	Jy beam ⁻¹	Local RMS at 122 MHz
113	peak_flux_122	Jy beam ⁻¹	Peak flux density at 122 MHz
114	err_peak_flux_122	Jy beam ⁻¹	Fitting error on peak flux density at 122 MHz
115	int_flux_122	Jy	Integrated flux density at 122 MHz
116	err_int_flux_122	Jy	Fitting error on integrated flux density at 122 MHz
117	a_122	//	Major axis of source at 122 MHz
118	b_122	//	Minor axis of source at 122 MHz
119	pa_122	°	Position angle of source at 122 MHz
120	residual_mean_122	Jy beam ⁻¹	Mean of residual after source fitting at 122 MHz
121	residual_std_122	Jy beam ⁻¹	Standard deviation of residual after source fitting at 122 MHz
122	psf_a_122	//	Major axis of PSF at location of source at 122 MHz
123	psf_b_122	//	Minor axis of PSF at location of source at 122 MHz
124	psf_pa_122	°	Position angle of PSF at location of source at 122 MHz
125	background_130	Jy beam ⁻¹	Background at 130 MHz
126	local_rms_130	Jy beam ⁻¹	Local RMS at 130 MHz
127	peak_flux_130	Jy beam ⁻¹	Peak flux density at 130 MHz
128	err_peak_flux_130	Jy beam ⁻¹	Fitting error on peak flux density at 130 MHz

Table A2. Continued

Number	Name	Unit	Description
129	int_flux_130	Jy	Integrated flux density at 130 MHz
130	err_int_flux_130	Jy	Fitting error on integrated flux density at 130 MHz
131	a_130	//	Major axis of source at 130 MHz
132	b_130	//	Minor axis of source at 130 MHz
133	pa_130	°	Position angle of source at 130 MHz
134	residual_mean_130	Jy beam ⁻¹	Mean of residual after source fitting at 130 MHz
135	residual_std_130	Jy beam ⁻¹	Standard deviation of residual after source fitting at 130 MHz
136	psf_a_130	//	Major axis of PSF at location of source at 130 MHz
137	psf_b_130	//	Minor axis of PSF at location of source at 130 MHz
138	psf_pa_130	°	Position angle of PSF at location of source at 130 MHz
139	background_143	Jy beam ⁻¹	Background at 143 MHz
140	local_rms_143	Jy beam ⁻¹	Local RMS at 143 MHz
141	peak_flux_143	Jy beam ⁻¹	Peak flux density at 143 MHz
142	err_peak_flux_143	Jy beam ⁻¹	Fitting error on peak flux density at 143 MHz
143	int_flux_143	Jy	Integrated flux density at 143 MHz
144	err_int_flux_143	Jy	Fitting error on integrated flux density at 143 MHz
145	a_143	//	Major axis of source at 143 MHz
146	b_143	//	Minor axis of source at 143 MHz
147	pa_143	°	Position angle of source at 143 MHz
148	residual_mean_143	Jy beam ⁻¹	Mean of residual after source fitting at 143 MHz
149	residual_std_143	Jy beam ⁻¹	Standard deviation of residual after source fitting at 143 MHz
150	psf_a_143	//	Major axis of PSF at location of source at 143 MHz
151	psf_b_143	//	Minor axis of PSF at location of source at 143 MHz
152	psf_pa_143	°	Position angle of PSF at location of source at 143 MHz
153	background_151	Jy beam ⁻¹	Background at 151 MHz
154	local_rms_151	Jy beam ⁻¹	Local RMS at 151 MHz
155	peak_flux_151	Jy beam ⁻¹	Peak flux density at 151 MHz
156	err_peak_flux_151	Jy beam ⁻¹	Fitting error on peak flux density at 151 MHz
157	int_flux_151	Jy	Integrated flux density at 151 MHz
158	err_int_flux_151	Jy	Fitting error on integrated flux density at 151 MHz
159	a_151	//	Major axis of source at 151 MHz
160	b_151	//	Minor axis of source at 151 MHz
161	pa_151	°	Position angle of source at 151 MHz
162	residual_mean_151	Jy beam ⁻¹	Mean of residual after source fitting at 151 MHz
163	residual_std_151	Jy beam ⁻¹	Standard deviation of residual after source fitting at 151 MHz
164	psf_a_151	//	Major axis of PSF at location of source at 151 MHz
165	psf_b_151	//	Minor axis of PSF at location of source at 151 MHz
166	psf_pa_151	°	Position angle of PSF at location of source at 151 MHz
167	background_158	Jy beam ⁻¹	Background at 158 MHz
168	local_rms_158	Jy beam ⁻¹	Local RMS at 158 MHz
169	peak_flux_158	Jy beam ⁻¹	Peak flux density at 158 MHz
170	err_peak_flux_158	Jy beam ⁻¹	Fitting error on peak flux density at 158 MHz
171	int_flux_158	Jy	Integrated flux density at 158 MHz
172	err_int_flux_158	Jy	Fitting error on integrated flux density at 158 MHz
173	a_158	//	Major axis of source at 158 MHz
174	b_158	//	Minor axis of source at 158 MHz

Table A2. Continued

Number	Name	Unit	Description
175	pa_158	°	Position angle of source at 158 MHz
176	residual_mean_158	Jy beam ⁻¹	Mean of residual after source fitting at 158 MHz
177	residual_std_158	Jy beam ⁻¹	Standard deviation of residual after source fitting at 158 MHz
178	psf_a_158	//	Major axis of PSF at location of source at 158 MHz
179	psf_b_158	//	Minor axis of PSF at location of source at 158 MHz
180	psf_pa_158	°	Position angle of PSF at location of source at 158 MHz
181	background_166	Jy beam ⁻¹	Background at 166 MHz
182	local_rms_166	Jy beam ⁻¹	Local RMS at 166 MHz
183	peak_flux_166	Jy beam ⁻¹	Peak flux density at 166 MHz
184	err_peak_flux_166	Jy beam ⁻¹	Fitting error on peak flux density at 166 MHz
185	int_flux_166	Jy	Integrated flux density at 166 MHz
186	err_int_flux_166	Jy	Fitting error on integrated flux density at 166 MHz
187	a_166	//	Major axis of source at 166 MHz
188	b_166	//	Minor axis of source at 166 MHz
189	pa_166	°	Position angle of source at 166 MHz
190	residual_mean_166	Jy beam ⁻¹	Mean of residual after source fitting at 166 MHz
191	residual_std_166	Jy beam ⁻¹	Standard deviation of residual after source fitting at 166 MHz
192	psf_a_166	//	Major axis of PSF at location of source at 166 MHz
193	psf_b_166	//	Minor axis of PSF at location of source at 166 MHz
194	psf_pa_166	°	Position angle of PSF at location of source at 166 MHz
195	background_174	Jy beam ⁻¹	Background at 174 MHz
196	local_rms_174	Jy beam ⁻¹	Local RMS at 174 MHz
197	peak_flux_174	Jy beam ⁻¹	Peak flux density at 174 MHz
198	err_peak_flux_174	Jy beam ⁻¹	Fitting error on peak flux density at 174 MHz
199	int_flux_174	Jy	Integrated flux density at 174 MHz
200	err_int_flux_174	Jy	Fitting error on integrated flux density at 174 MHz
201	a_174	//	Major axis of source at 174 MHz
202	b_174	//	Minor axis of source at 174 MHz
203	pa_174	°	Position angle of source at 174 MHz
204	residual_mean_174	Jy beam ⁻¹	Mean of residual after source fitting at 174 MHz
205	residual_std_174	Jy beam ⁻¹	Standard deviation of residual after source fitting at 174 MHz
206	psf_a_174	//	Major axis of PSF at location of source at 174 MHz
207	psf_b_174	//	Minor axis of PSF at location of source at 174 MHz
208	psf_pa_174	°	Position angle of PSF at location of source at 174 MHz
209	background_181	Jy beam ⁻¹	Background at 181 MHz
210	local_rms_181	Jy beam ⁻¹	Local RMS at 181 MHz
211	peak_flux_181	Jy beam ⁻¹	Peak flux density at 181 MHz
212	err_peak_flux_181	Jy beam ⁻¹	Fitting error on peak flux density at 181 MHz
213	int_flux_181	Jy	Integrated flux density at 181 MHz
214	err_int_flux_181	Jy	Fitting error on integrated flux density at 181 MHz
215	a_181	//	Major axis of source at 181 MHz
216	b_181	//	Minor axis of source at 181 MHz
217	pa_181	°	Position angle of source at 181 MHz
218	residual_mean_181	Jy beam ⁻¹	Mean of residual after source fitting at 181 MHz
219	residual_std_181	Jy beam ⁻¹	Standard deviation of residual after source fitting at 181 MHz
220	psf_a_181	//	Major axis of PSF at location of source at 181 MHz

Table A2. Continued

Number	Name	Unit	Description
221	psf_b_181	//	Minor axis of PSF at location of source at 181 MHz
222	psf_pa_181	°	Position angle of PSF at location of source at 181 MHz
223	background_189	Jy beam ⁻¹	Background at 189 MHz
224	local_rms_189	Jy beam ⁻¹	Local RMS at 189 MHz
225	peak_flux_189	Jy beam ⁻¹	Peak flux density at 189 MHz
226	err_peak_flux_189	Jy beam ⁻¹	Fitting error on peak flux density at 189 MHz
227	int_flux_189	Jy	Integrated flux density at 189 MHz
228	err_int_flux_189	Jy	Fitting error on integrated flux density at 189 MHz
229	a_189	//	Major axis of source at 189 MHz
230	b_189	//	Minor axis of source at 189 MHz
231	pa_189	°	Position angle of source at 189 MHz
232	residual_mean_189	Jy beam ⁻¹	Mean of residual after source fitting at 189 MHz
233	residual_std_189	Jy beam ⁻¹	Standard deviation of residual after source fitting at 189 MHz
234	psf_a_189	//	Major axis of PSF at location of source at 189 MHz
235	psf_b_189	//	Minor axis of PSF at location of source at 189 MHz
236	psf_pa_189	°	Position angle of PSF at location of source at 189 MHz
237	background_197	Jy beam ⁻¹	Background at 197 MHz
238	local_rms_197	Jy beam ⁻¹	Local RMS at 197 MHz
239	peak_flux_197	Jy beam ⁻¹	Peak flux density at 197 MHz
240	err_peak_flux_197	Jy beam ⁻¹	Fitting error on peak flux density at 197 MHz
241	int_flux_197	Jy	Integrated flux density at 197 MHz
242	err_int_flux_197	Jy	Fitting error on integrated flux density at 197 MHz
243	a_197	//	Major axis of source at 197 MHz
244	b_197	//	Minor axis of source at 197 MHz
245	pa_197	°	Position angle of source at 197 MHz
246	residual_mean_197	Jy beam ⁻¹	Mean of residual after source fitting at 197 MHz
247	residual_std_197	Jy beam ⁻¹	Standard deviation of residual after source fitting at 197 MHz
248	psf_a_197	//	Major axis of PSF at location of source at 197 MHz
249	psf_b_197	//	Minor axis of PSF at location of source at 197 MHz
250	psf_pa_197	°	Position angle of PSF at location of source at 197 MHz
251	background_204	Jy beam ⁻¹	Background at 204 MHz
252	local_rms_204	Jy beam ⁻¹	Local RMS at 204 MHz
253	peak_flux_204	Jy beam ⁻¹	Peak flux density at 204 MHz
254	err_peak_flux_204	Jy beam ⁻¹	Fitting error on peak flux density at 204 MHz
255	int_flux_204	Jy	Integrated flux density at 204 MHz
256	err_int_flux_204	Jy	Fitting error on integrated flux density at 204 MHz
257	a_204	//	Major axis of source at 204 MHz
258	b_204	//	Minor axis of source at 204 MHz
259	pa_204	°	Position angle of source at 204 MHz
260	residual_mean_204	Jy beam ⁻¹	Mean of residual after source fitting at 204 MHz
261	residual_std_204	Jy beam ⁻¹	Standard deviation of residual after source fitting at 204 MHz
262	psf_a_204	//	Major axis of PSF at location of source at 204 MHz
263	psf_b_204	//	Minor axis of PSF at location of source at 204 MHz
264	psf_pa_204	°	Position angle of PSF at location of source at 204 MHz
265	background_212	Jy beam ⁻¹	Background at 212 MHz
266	local_rms_212	Jy beam ⁻¹	Local RMS at 212 MHz
267	peak_flux_212	Jy beam ⁻¹	Peak flux density at 212 MHz

Table A2. Continued

Number	Name	Unit	Description
268	err_peak_flux_212	Jy beam ⁻¹	Fitting error on peak flux density at 212 MHz
269	int_flux_212	Jy	Integrated flux density at 212 MHz
270	err_int_flux_212	Jy	Fitting error on integrated flux density at 212 MHz
271	a_212	//	Major axis of source at 212 MHz
272	b_212	//	Minor axis of source at 212 MHz
273	pa_212	°	Position angle of source at 212 MHz
274	residual_mean_212	Jy beam ⁻¹	Mean of residual after source fitting at 212 MHz
275	residual_std_212	Jy beam ⁻¹	Standard deviation of residual after source fitting at 212 MHz
276	psf_a_212	//	Major axis of PSF at location of source at 212 MHz
277	psf_b_212	//	Minor axis of PSF at location of source at 212 MHz
278	psf_pa_212	°	Position angle of PSF at location of source at 212 MHz
279	background_220	Jy beam ⁻¹	Background at 220 MHz
280	local_rms_220	Jy beam ⁻¹	Local RMS at 220 MHz
281	peak_flux_220	Jy beam ⁻¹	Peak flux density at 220 MHz
282	err_peak_flux_220	Jy beam ⁻¹	Fitting error on peak flux density at 220 MHz
283	int_flux_220	Jy	Integrated flux density at 220 MHz
284	err_int_flux_220	Jy	Fitting error on integrated flux density at 220 MHz
285	a_220	//	Major axis of source at 220 MHz
286	b_220	//	Minor axis of source at 220 MHz
287	pa_220	°	Position angle of source at 220 MHz
288	residual_mean_220	Jy beam ⁻¹	Mean of residual after source fitting at 220 MHz
289	residual_std_220	Jy beam ⁻¹	Standard deviation of residual after source fitting at 220 MHz
290	psf_a_220	//	Major axis of PSF at location of source at 220 MHz
291	psf_b_220	//	Minor axis of PSF at location of source at 220 MHz
292	psf_pa_220	°	Position angle of PSF at location of source at 220 MHz
293	background_227	Jy beam ⁻¹	Background at 227 MHz
294	local_rms_227	Jy beam ⁻¹	Local RMS at 227 MHz
295	peak_flux_227	Jy beam ⁻¹	Peak flux density at 227 MHz
296	err_peak_flux_227	Jy beam ⁻¹	Fitting error on peak flux density at 227 MHz
297	int_flux_227	Jy	Integrated flux density at 227 MHz
298	err_int_flux_227	Jy	Fitting error on integrated flux density at 227 MHz
299	a_227	//	Major axis of source at 227 MHz
300	b_227	//	Minor axis of source at 227 MHz
301	pa_227	°	Position angle of source at 227 MHz
302	residual_mean_227	Jy beam ⁻¹	Mean of residual after source fitting at 227 MHz
303	residual_std_227	Jy beam ⁻¹	Standard deviation of residual after source fitting at 227 MHz
304	psf_a_227	//	Major axis of PSF at location of source at 227 MHz
305	psf_b_227	//	Minor axis of PSF at location of source at 227 MHz
306	psf_pa_227	°	Position angle of PSF at location of source at 227 MHz
307	background_W_087	Jy beam ⁻¹	Background at 072–103 MHz
308	local_rms_W_087	Jy beam ⁻¹	Local RMS at 072–103 MHz
309	peak_flux_W_087	Jy beam ⁻¹	Peak flux density at 072–103 MHz
310	err_peak_flux_W_087	Jy beam ⁻¹	Fitting error on peak flux density at 072–103 MHz
311	int_flux_W_087	Jy	Integrated flux density at 072–103 MHz
312	err_int_flux_W_087	Jy	Fitting error on integrated flux density at 072–103 MHz
313	a_W_087	//	Major axis of source at 072–103 MHz

Table A2. Continued

Number	Name	Unit	Description
314	b_W_087	//	Minor axis of source at 072–103 MHz
315	pa_W_087	°	Position angle of source at 072–103 MHz
316	residual_mean_W_087	Jy beam ⁻¹	Mean of residual after source fitting at 072–103 MHz
317	residual_std_W_087	Jy beam ⁻¹	Standard deviation of residual after source fitting at 072–103 MHz
318	psf_a_W_087	//	Major axis of PSF at location of source at 072–103 MHz
319	psf_b_W_087	//	Minor axis of PSF at location of source at 072–103 MHz
320	psf_pa_W_087	°	Position angle of PSF at location of source at 072–103 MHz
321	background_W_118	Jy beam ⁻¹	Background at 103–134 MHz
322	local_rms_W_118	Jy beam ⁻¹	Local RMS at 103–134 MHz
323	peak_flux_W_118	Jy beam ⁻¹	Peak flux density at 103–134 MHz
324	err_peak_flux_W_118	Jy beam ⁻¹	Fitting error on peak flux density at 103–134 MHz
325	int_flux_W_118	Jy	Integrated flux density at 103–134 MHz
326	err_int_flux_W_118	Jy	Fitting error on integrated flux density at 103–134 MHz
327	a_W_118	//	Major axis of source at 103–134 MHz
328	b_W_118	//	Minor axis of source at 103–134 MHz
329	pa_W_118	°	Position angle of source at 103–134 MHz
330	residual_mean_W_118	Jy beam ⁻¹	Mean of residual after source fitting at 103–134 MHz
331	residual_std_W_118	Jy beam ⁻¹	Standard deviation of residual after source fitting at 103–134 MHz
332	psf_a_W_118	//	Major axis of PSF at location of source at 103–134 MHz
333	psf_b_W_118	//	Minor axis of PSF at location of source at 103–134 MHz
334	psf_pa_W_118	//	Position angle of PSF at location of source at 103–134 MHz
335	background_W_154	Jy beam ⁻¹	Background at 139–170 MHz
336	local_rms_W_154	Jy beam ⁻¹	Local RMS at 139–170 MHz
337	peak_flux_W_154	Jy beam ⁻¹	Peak flux density at 139–170 MHz
338	err_peak_flux_W_154	Jy beam ⁻¹	Fitting error on peak flux density at 139–170 MHz
339	int_flux_W_154	Jy	Integrated flux density at 139–170 MHz
340	err_int_flux_W_154	Jy	Fitting error on integrated flux density at 139–170 MHz
341	a_W_154	//	Major axis of source at 139–170 MHz
342	b_W_154	//	Minor axis of source at 139–170 MHz
343	pa_W_154	°	Position angle of source at 139–170 MHz
344	residual_mean_W_154	Jy beam ⁻¹	Mean of residual after source fitting at 139–170 MHz
345	residual_std_W_154	Jy beam ⁻¹	Standard deviation of residual after source fitting at 139–170 MHz
346	psf_a_W_154	//	Major axis of PSF at location of source at 139–170 MHz
347	psf_b_W_154	//	Minor axis of PSF at location of source at 139–170 MHz
348	psf_pa_W_154	//	Position angle of PSF at location of source at 139–170 MHz
349	background_W_185	Jy beam ⁻¹	Background at 170–200 MHz
350	local_rms_W_185	Jy beam ⁻¹	Local RMS at 170–200 MHz
351	peak_flux_W_185	Jy beam ⁻¹	Peak flux density at 170–200 MHz
352	err_peak_flux_W_185	Jy beam ⁻¹	Fitting error on peak flux density at 170–200 MHz
353	int_flux_W_185	Jy	Integrated flux density at 170–200 MHz
354	err_int_flux_W_185	Jy	Fitting error on integrated flux density at 170–200 MHz
355	a_W_185	//	Major axis of source at 170–200 MHz
356	b_W_185	//	Minor axis of source at 170–200 MHz
357	pa_W_185	°	Position angle of source at 170–200 MHz
358	residual_mean_W_185	Jy beam ⁻¹	Mean of residual after source fitting at 170–200 MHz
359	residual_std_W_185	Jy beam ⁻¹	Standard deviation of residual after source fitting at 170–200 MHz

Table A2. Continued

Number	Name	Unit	Description
360	psf_a_W_185	"	Major axis of PSF at location of source at 170–200 MHz
361	psf_b_W_185	"	Minor axis of PSF at location of source at 170–200 MHz
362	psf_pa_W_185	"	Position angle of PSF at location of source at 170–200 MHz
363	background_W_215	Jy beam ⁻¹	Background at 200–231 MHz
364	local_rms_W_215	Jy beam ⁻¹	Local RMS at 200–231 MHz
365	peak_flux_W_215	Jy beam ⁻¹	Peak flux density at 200–231 MHz
366	err_peak_flux_W_215	Jy beam ⁻¹	Fitting error on peak flux density at 200–231 MHz
367	int_flux_W_215	Jy	Integrated flux density at 200–231 MHz
368	err_int_flux_W_215	Jy	Fitting error on integrated flux density at 200–231 MHz
369	a_W_215	"	Major axis of source at 200–231 MHz
370	b_W_215	"	Minor axis of source at 200–231 MHz
371	pa_W_215	°	Position angle of source at 200–231 MHz
372	residual_mean_W_215	Jy beam ⁻¹	Mean of residual after source fitting at 200–231 MHz
373	residual_std_W_215	Jy beam ⁻¹	Standard deviation of residual after source fitting at 200–231 MHz
374	psf_a_W_215	"	Major axis of PSF at location of source at 200–231 MHz
375	psf_b_W_215	"	Minor axis of PSF at location of source at 200–231 MHz
376	psf_pa_W_215	"	Position angle of PSF at location of source at 200–231 MHz
377	sp_int_flux_fit_200	Jy	Power-law fitted flux density at 200 MHz
378	err_sp_int_flux_fit_200	Jy	Error on power-law fitted flux density at 200 MHz
379	sp_alpha	–	Fitted spectral index assuming a power-law SED
380	err_sp_alpha	–	Error on power-law fitted spectral index
381	sp_reduced_chi2	–	Reduced χ^2 statistic for power-law SED fit
382	csp_int_flux_fit_200	Jy	Curved SED fitted flux density at 200 MHz
383	err_csp_int_flux_fit_200	Jy	Error on curved SED fitted flux density at 200 MHz
384	csp_alpha	–	Fitted spectral index assuming a curved SED
385	err_csp_alpha	–	Error on curved SED fitted spectral index
386	csp_beta	–	Fitted curvature index for curved SED fit
387	err_csp_beta	–	Error on curvature index for curved SED fit
388	csp_reduced_chi2	–	Reduced χ^2 statistic for curved SED fit